This is the peer-reviewed, final accepted version for American Mineralogist, published by the Mineralogical Society of America.
The published version is subject to change. Cite as Authors (Year) Title. American Mineralogist, in press.
DOI: https://doi.org/10.2138/am-2021-7881. http://www.minsocam.org/

Revision 1

Release of chromite nanoparticles and their alteration in the presence of Mn-oxides

Neal W. McClenaghan[1] and Michael Schindler[2]*

1. Harquail School of Earth Sciences, Laurentian University, Sudbury, ON, P3E2C6, Canada, e-mail: nmcclenaghan@laurentian.ca

2. Department of Geological Sciences, University of Manitoba, Winnipeg, MB, R3T2N2, Canada

*Corresponding author: Michael.schindler@umanitoba.ca

This is the peer-reviewed, final accepted version for American Mineralogist, published by the Mineralogical Society of America.
The published version is subject to change. Cite as Authors (Year) Title. American Mineralogist, in press.
DOI: https://doi.org/10.2138/am-2021-7881. http://www.minsocam.org/

Abstract

The discovery of chromite nanoparticles in silicates of ultramafic rocks may change our approach on the environmental risk assessment of mine waste associated with chromitite mining. This experimental study shows for the first time that the alteration of Cr-rich silicates results in the release of chromite nanoparticles and that their interaction with oxidizing Mn-oxide nanoparticles causes the dissolution of chromite and Mn-oxide nanoparticles and the precipitation of Fe^{3+}- and Cr^{3+}-hydroxides. Transmission electron microscopy (TEM) in combination with ultra-microtomy, centrifugation, chromatography, ICP-MS and UV-VIS is used to characterize release and alteration of chromite nanoparticles and the concentrations and speciation of Cr aqueous species. Alteration of clinochlore grains containing chromite nanoparticles results in the release of the nanoparticles and their attachment to Si-bearing Al-hydroxide colloids. Chromite nanoparticles with the endmember composition $FeCr_2O_4$ are synthesized and their interaction with Mn-oxide nanoparticles (hausmannite, Mn_3O_4), Fe^{2+}-silicates (chamosite, $[(Fe_{3.9}Mg_{0.62}Al_{0.48})\ Al(Si_3Al)O_{10}(OH)_8]$ and organic matter is studied over a period of six to nine months in suspensions of pH = 5. The interaction of chromite and hausmannite nanoparticles is facilitated by the aggregation of the nanoparticles and dissolution-precipitation processes. Processes on the surfaces of the hausmannite nanoparticles include the reductive dissolution of the substrate (reduction of Mn^{3+} to Mn^{2+} by Fe^{2+} species) and its replacement by amorphous or nanocrystalline Cr^{3+}-bearing Fe^{3+}-hydroxides. Processes on the surfaces of the chromite nanoparticles involve the attachment of hausmannite nanoparticles, the oxidative dissolution of the substrate (oxidation of Fe^{2+} and perhaps Cr^{3+} by Mn^{3+} species), its replacement by an amorphous or nanocrystalline Mn-bearing Cr^{3+}-hydroxide matrix and the formation of the Cr^{3+}-hydroxides bracewellite and grimaldite within the latter matrix. Analyses

of the suspensions indicate only minor amounts of Cr^{6+} in the suspensions (< 5 µg kg^{-1}) suggesting that formation or occurrence of Cr^{6+} species can be limited in complex geochemical and mineralogical systems, even in the presence of hausmannite nanoparticles.

This is the peer-reviewed, final accepted version for American Mineralogist, published by the Mineralogical Society of America.
The published version is subject to change. Cite as Authors (Year) Title. American Mineralogist, in press.
DOI: https://doi.org/10.2138/am-2021-7881. http://www.minsocam.org/

Introduction

The environmental fate and toxicity of Cr strongly depends on local redox and pH conditions as Cr^{3+}-bearing minerals and aqueous species have commonly a lower solubility and mobility than their Cr^{6+}-bearing toxic counterparts (Fendorf and Zasoski, 1992; Oliveira, 2012). The only known naturally occurring oxidizing agents of Cr^{3+} are Mn-oxides (Fendorf and Zasoski, 1992; Weaver and Hochella, 2003). Studies on the oxidation and reduction of Cr^{3+} and Cr^{6+} species in the presence and absence of Mn-oxides indicate that (1) Cr^{3+} oxidation to Cr^{6+} in the presence of Mn-oxides is rapid around pH = 5, but as Cr^{3+} concentration and pH increase the reaction become limited; (2) products of the oxidation of Cr^{3+} are commonly Mn^{2+} and Cr^{6+} which both do not limit the oxidation of Cr^{3+} through a shift in the redox potential or equilibrium; (3) Mn-oxides with the greatest and longest lasting oxidizing ability are those that contain both Mn^{3+} and Mn^{2+}; (4) a higher proportion of Cr^{6+} forms in chromite-bearing serpentinite soils in the presence than absence of birnessite, MnO_2; (5) Cr^{6+} can be reduced by various substances including organic matter, Fe^{2+} and sulfides and (6) the formation of Cr^{6+} can be suppressed by organic matter, even in the presence of Mn-oxides (Fendorf and Zasoski, 1992; Weaver and Hochella, 2003; Oze et al. 2007; Jiang et al., 2014; Hausladen and Fendorf 2017). Recently, Pan et al. (2017, 2019) conducted multichamber experiments in order to assess the oxidation of Cr^{3+} to Cr^{6+} in the absence of solid-solid interactions. In these experiments, Cr^{3+} aqueous species or Cr^{3+}-Fe^{3+} hydroxides were spatially separated from MnO_2 particles, while aqueous species transport could still occur across a permeable membrane. The authors showed that (a) oxidation of Cr^{3+} to Cr^{6+} occurred on the surface of MnO_2 particles, (b) Cr^{6+} production rates were much lower in multichamber than in completely mixed batch experiments, (i.e. with solid-solid interaction between Cr^{3+}-Fe^{3+}-hydroxides and birnessite, Mn_3O_4) (c) Cr^{3+} oxidation

rate was initially fast, but then slowed and ceased in solutions with pH-values of 5 to 7. Serpentinite soils and laterites derived from ultramafic rocks are typically enriched in Cr (up to 80 600 mg/kg Cr) (Fendorf and Zasoski, 1992; Godgul and Sahu, 1995; Oze et al., 2004; Oze et al., 2007) and can contain Cr^{6+} -species in the presence of Mn-oxides (Fandeur et al. 2009). Chromium (VI) has been also detected in natural solutions in proximity to ophiolite complexes (Robles-Camacho and Armienta, 2000; Ball and Izbicki, 2004; Manning et al., 2015; Morrison et al., 2015).

The discovery of chromite nanoparticles within clinochlore and lizardite grains in chromitite ore from the Black Thor chromium deposit in central Canada and the Mistake mine, part of the Franciscan ophiolite complex, California, USA adds an unforeseen complexity to the mineralogy and geochemistry of Cr in serpentinite soils (Schindler et al. 2017) as it was commonly assumed that Cr^{3+} is structurally incorporated into silicate minerals containing octahedral chains and layers (Roy and Roy, 1954; Huebner et al., 1976; Cameron and Papike 1981; Mével and Kienast, 1986; Phillips et al. 1980; Platonov et al. 1996). Schindler et al. (2017) argued that the release of Cr during the weathering of the silicate minerals may occur in the form of chromite nanoparticles rather than Cr^{3+}-aqueous species. In this case, the environmental fate of the element will be governed by the specific properties of the nanoparticles such as their reactivity, solubility and their abilities to aggregate or to adhere to mineral surfaces (Hochella et al., 2008; Theng and Yuan 2008; Hotze et al. 2010; Kumar, et al. 2012; Kaptay, 2012; Aliofkhazraei et al., 2016). The chromite nanoparticles in the silicates are 3-5 nm in diameter, occur in random orientations throughout the host silicates, are released during the weathering of their host silicates and most likely adhere to other nanoparticles present in solution (Schindler et al. 2017).

Schindler et al (2018) studied dissolution mechanisms of chromite and clinochlore in chromitite samples under acidic, near neutral and basic pH conditions in the absence and presence of Fe-oxidizing bacteria. The authors showed that dissolution of chromitite is non-stochiometric and results in surfaces enriched in Fe and Si relative to Cr.

Objectives

An understanding of the fate of chromite nanoparticles in the environment requires knowledge about their interactions with other nanoparticles, mineral surfaces and redox-sensitive components in the soil environment such as Mn-oxides and organic matter. This interaction includes the pathways for the potential oxidation of Cr^{3+} and Fe^{2+} by Mn-oxides; *i.e.*

(a) do redox processes occur along common interfaces between chromite and Mn-oxide nanoparticles, as previous experiments indicate high rates of Cr^{3+} oxidation through Cr^{3+}-Fe^{3+}-hydroxide-birnessite solid-solid interactions (Pan et al. 2017)? If yes, do they involve dissolution-reprecipitation processes and what are the secondary phases formed during these processes?

(b) Do similar interfacial processes occur in the presence of reductive solids common in chromite-ore deposits and surrounding soils such as Fe^{2+}-bearing chlorites and organic-rich soils?

Hence, the objectives of this experimental study are to examine release of chromite nanoparticles during the breakdown of their silicate hosts and to identify the underlying mechanisms for interfacial redox processes involving nanoparticles of chromite and hausmannite and other constituents most likely present in serpentinite soils. These goals will be

achieved in experimental studies through conducting two distinct analytical and experimental approaches:

I. Leaching of a silicate-enriched fraction of a chromitite ore sample in solutions of pH = 2 and pH = 5 in combination with TEM-STEM-EDS analyses in order to determine whether chromite nanoparticles are released and stable upon the weathering of their silicate hosts. The chromitite ore sample is from the Black Thor deposit Chromium deposit and the abundance of chromite nanoparticles in clinochlore grains present in the ore have been determined by Schindler et al. (2017). A silicate-enriched fraction is prepared to increase the modal abundance of clinochlore (and thus of the chromite nanoparticles) and to simulate better the weathering of mine waste composed of Cr-bearing silicates, which will be most likely a finely-grained material composed of silica-rich gangue material. The pH-value of pH =5 is chosen as the eutric brunisolic soils surrounding the Black Thor chromium deposit have contact pH-values of pH = 4.5 to 5.0 on the surface and pH > 5.5 at greater depth (Smith et al. 2011). The pH value of pH = 2 is selected as changes in surface chemistry of chromitites under these pH conditions have been well characterized (see above, Schindler et al. 2018).

II. Long-term (six to nine months) batch experiments in combination with TEM-STEM-EDS in order to characterize the alteration of synthesized chromite nanoparticles (endmember composition $FeCr_2O_4$) in the presence of other components most likely present in serpentinite soils such as hausmannite, Mn_3O_4 nanoparticles, chamosite (an Fe^{2+}-rich mineral of the chlorite group) and organic-rich soils. Although birnessite shows commonly a stronger ability to oxidize Cr^{3+} to Cr^{6+} than other Mn-oxides, we select hausmannite for our experiment as the oxidization of Cr^{3+} to Cr^{6+} (a) strongly depends on the crystallinity

of the birnessite sample and (b) is sustained over a longer period of time in the presence of hausmannite than birnessite (Weaver and Hochella 2003). The concentrations of Cr_{total}, Cr^{3+}, Cr^{6+}, Mn and Fe will be determined with ICP-MS and combinations of chromatography/ICP-MS and chromatography/UV-VIS.

Although these two approaches involve complex chemical and mineralogical systems, which do not allow the identification of individual parameters affecting the oxidative dissolution rates of chromite nanoparticles, we believe that they provide a good simulation on the interaction of chromite nanoparticles with components in mine waste and adjacent soils around the Ring of Fire. This can be understood when considering that

I. Clinochlore and sulfides are common minerals of the ore deposit (Laarman, 2013) and a fine-grained silicate-rich fraction composed of Cr-bearing clinochlore will most likely interact with sulfuric-acid solutions in potential waste disposal site around the Ring of Fire;

II. Fine-grained powders of chamosite and an organic-rich soil from Northern Ontario may represent reductive environments in and around potential mine waste site. The addition of maximum 50 mgL^{-1} phosphate in the form of a KH_2PO_4 buffer to the experiments (see below) may simulate expected P-concentrations in pore waters of soils in Northern Ontario (~10 mgL^{-1} for e.g. organic rich soils (Griffiths et al. 2019) and ~70 mgL^{-1} for agricultural used soils (Amarawansha et al. 2015)).

Materials and Methods

Leaching experiments of a silicate-enriched fraction of a chromitite ore sample

Chromitite samples from the Black Thor chromite deposit, Ontario, Canada were obtained from Ontario Geological Survey. A silicate-enriched fraction of this ore with a circa 7-times lower Cr : Si ratio (Table 1) was obtained through heavy-mineral fractionation (Wilfley Table) from a powdered sample with a grain size ranging from 10 to 100µm. Two-hundred milligram of the silicate-enriched fraction was subsequently leached with 50 ml sulfuric acid solutions of pH = 2 and pH = 5. After three months continuous shaking in test tubes, the chemical compositions of the leachates were characterized with ICP-MS (Table 2) and parts of their colloidal fractions were deposited on TEM grids via centrifugation and characterized with TEM (see below).

Set up of the long-term batch experiments

Six long-term (six to nine months) batch experiments were set up to examine the interaction between chromite and hausmannite nanoparticles in the presence and absence of chamosite and organic-rich soil. The experiments were conducted in 500 mL flasks with a Cr-concentration of 0.01 mol/L and Cr : Mn molar ratios of either 1 : 1 or 1 : 5 (Table S2). Two of these experiments included 10g chamosite powder and two included 10g of the organic-rich soil (Table S2, S = supplementary data). The pH-values in the long-term batch experiments were adjusted to a pH value of pH = 5.0 with sulfuric acid and at a later stage with a 0.1 $molL^{-1}$ KH_2PO_4 solution (after one month, max. 8 ml or 50 mgL^{-1} P) and a 0.05 $molL^{-1}$ solution of Potassium hydrogen phthalate solution (after every month until the end of the experiment, maximum 32 mL or 1.6 mmol).

206 Over the course of the experiments, the Eh-pH values were monitored with a YSI ORP
207 probe and a pH meter. Probe and pH meter contain standard hydrogen electrodes which were
208 calibrated against pH solutions of pH 4, 7 and 10 and a K-iodide standard. The standard
209 deviation of individual measurement pH and Eh measurements is circa ± 0.2 units, based on
210 repeated measurements of the standard solutions.
211 After 6- and 9-months continuous shaking of the 500 ml flasks, 10 mL of the suspensions
212 were extracted, centrifuged, filtered and analysed for their chemical composition, respectively
213 (see below).
214 Additional information on the reagents (synthesized chromite nanoparticles, chamosite,
215 organic matter, hausmannite nanoparticles) used in the long-term batch can be found in the
216 supplementary data (Table S1, Fig. S1-S4). The supplementary data also lists the analytical
217 protocols for all chemical analyses.
218
219 *Preparation of the TEM samples*
220 The colloidal fractions of the solutions after the leaching experiment and the long-term
221 batch experiments were also deposited on TEM grids. Here, Cu TEM grids (400 mesh lacey
222 carbon, 100μm) were fixed to an epoxy support at the bottom of 15ml centrifuge tubes and then
223 filled with the leachates extracted from the test tubes. The tubes were centrifuged using a Sorvall
224 ST16 centrifuge equipped with a TX-400 swing bucket rotor for 8 hours at 5000 RPM which,
225 according to stokes equation, will deposit all spherical particles with densities and diameters
226 greater than 4.54 g cm^{-3} (density of chromite) and 30 nm onto the TEM grids, respectively.
227
228

Scanning electron microscopy and Transmission Electron Microscopy,

Scanning electron microscopy on polished chromitite grains embedded in epoxy pucks (Table 1) was conducted with a JEOL 6400 SEM, which was operated with an accelerating voltage of 20 kV and a beam current of 1 nA, in combination with energy dispersive X-ray spectrometry (EDS).

The TEM grids with deposited colloids/nanoparticles were examined with a field emission Transmission Electron Microscope FEI Talos F200x at the Manitoba Institute of Materials. An accelerating voltage of 200 kV in bright and dark field mode was used with a 16MB ceta camera and Fischicone annular dark field (HAADF) detector to acquire images and SAED.

RESULTS

The results of the nano-mineralogical and chemical study of the suspensions after leaching of the silicate-enriched fraction of a chromitite sample will be addressed first followed by the characterization of the suspensions after the six to nine months long-term batch experiments.

Chemical and mineralogical composition of the colloids and solutions after leaching of the silicate-enriched fraction

After three months leaching of the silicate-enriched fraction of the chromitite ore sample, the solution of pH = 2 has higher concentrations of all major elements (Mg, Al, Fe, Cr and Si) than the solution of pH = 5. Higher concentrations of Al, Si and Mg relative Fe and Cr in both leachates indicate higher dissolution rates of clinochlore relative to chromite. The lower Al/Si

252 ratios in the leachates of pH = 2 and pH = 5 than in the solid materials (Tables 1 and 2) indicate
253 non-stochiometric dissolution of mainly clinochlore. The higher Cr/Si atomic ratio in the
254 leachates of pH = 2 than pH =5 also suggests that the differences in dissolution rates between
255 clinochlore and chromite is higher at pH = 5 than pH = 2.

256 SEM examination of the silicate-enriched fraction show that chromite grains are slightly
257 chemically altered whereas the majority of the clinochlore grains are extensively etched (Fig.
258 1a). TEM examinations of the colloidal fraction in the leachates of pH = 2 and pH = 5 did not
259 unequivocally identify individual chromite nanoparticles on the TEM grids. Chromite
260 nanoparticles were only identified in larger clinochlore fragments (Fig. S5) and on the surface of
261 an Al-rich colloid with an elemental Al : Si : Cr : Fe ratio of ~8 : 2 : 1 : 1 and no detectable
262 concentrations of Mg (Fig. 1b-d, Fig. S6). Contrary, the colloidal fraction of the leachate of pH =
263 2 is composed of many Cr-, Fe- and Si rich colloids with diameters in the lower nanometer-size
264 range (Fig. 1e, f).

265

266 **Chemical and mineralogical features of the colloidal fraction in the suspensions after 6**
267 **months of the long-term batch experiments**

268 Different nanoparticle-adsorbed solute, nanoparticle-nanoparticle and nanoparticle-
269 microparticle interactions occur in the suspensions. The most notable interaction is the
270 aggregation of chromite and hausmannite nanoparticles (Fig. 2a-b). STEM chemical distribution
271 maps indicate that this aggregation process occurred in the presence of adsorbed phosphate
272 species (in red in Fig. 2b), which originated (most likely) from the KH_2PO_4 buffer added to the
273 solution (max. 50 mgL^{-1} P).

274

This is the peer-reviewed, final accepted version for American Mineralogist, published by the Mineralogical Society of America.
The published version is subject to change. Cite as Authors (Year) Title. American Mineralogist, in press.
DOI: https://doi.org/10.2138/am-2021-7881. http://www.minsocam.org/

Chemical trends among the nano- to micrometer-size particles

Scanning TEM-EDS chemical analyses of chromite nanoparticles or aggregates of chromite nanoparticles from the suspensions of all long-term batch experiments indicate that (altered) chromite nanoparticles are depleted in Fe and enriched in Mn relative to the synthesized chromite nanoparticles (Fig. 3a). Similarly, altered hausmannite nanoparticles are enriched in Fe and sometimes in Cr with maximum Fe : Mn and Cr : Mn ratios of 1 : 1 and 1 : 3, respectively (Fig 3b). Alterations also occur on the surfaces of the chamosite particles. These are commonly characterized by areas depleted in Mg and enriched in Al and Fe relative to the unaltered grains (Fig. 3c).

Textural, chemical and mineralogical features of chromite-hausmannite nanoparticle aggregates

Figure 4 shows a small aggregate of two altered hausmannite nanoparticles (see also Fig. S7) and the remains of a chromite nanoparticle from the suspension with the organic-rich soil (experiment 5). The hausmannite nanoparticles are enriched in Fe (Mn : Fe ratio ~1, Fig. 4b) and are highly altered with etch features at the lower nanometer range (dark spots in Fig. 4a). The distribution of Fe is heterogeneous with high abundances of Fe occurring in cracks and on the surface of the hausmannite nanoparticles (in red in Fig. 4c). The latter nanoparticles contain also pockets enriched in Si (in yellow in Fig. 4d) which often overlap or are adjacent to areas enriched in Fe. The remains of a chromite nanoparticle occur below the plane of the hausmannite nanoparticles (Fig. 4a and in green in Fig. 4b) and are depleted in Fe relative to an unaltered chromite nanoparticle (Fe : Cr ratio = 1 : 5).

Large aggregates of hausmannite nanoparticles with attached chromite nanoparticles occur in all suspensions. For example, a micrometer-size aggregate from the suspension with the

298 chamosite powder (experiment 3) contains highly altered hausmannite nanoparticles enriched in
299 Fe (max. Fe : Mn ratios of 1 : 1) along its surface and relatively unaltered nanoparticles in its
300 interior (Fig. 5a-b). The altered hausmannite nanoparticles are rimmed by a nanometer-thick
301 Fe(hydr)oxide precipitate without any apparent lattice fringes (Fig. 5c-d). Chromite
302 nanoparticles attached to the aggregate are also rimmed by Fe-(hydr)oxide precipitates (Fig. 5c)
303
304 *Textural, chemical and mineralogical features of secondary Cr-hydroxide phases*
305 Chromium (hydr)oxide precipitates occur in all suspensions. For example, precipitates in
306 the suspension with organic rich soil (experiment 6) are depleted in Fe and enriched in Mn
307 relative to chromite (min. Fe : Cr ratios ~ 1 : 14; max. Mn : Cr ratios of 1 : 7; Fig. 6). The
308 precipitates lack any apparent long- or short-range ordering (i.e. no diffraction spots in SAED
309 pattern and lattice fringes, Fig. S8) but their matrices contain rods of bracewellite (γ-CrO(OH))
310 (Fig. 6 and S8). In some cases, the morphology of the Cr-hydroxide precipitate resembles those
311 of a chromite cubo-octahedron with almost equi-dimensions (120 nm x 100 nm) (Fig.6d, e).
312 Hausmannite nanoparticles associated with the Cr-hydroxides precipitates are commonly
313 rimed by pockets of Mn-bearing Fe-(hydr)oxide precipitates (Fe : Mn ratios vary from 1 : 7 to 1 :
314 1; in red in Fig. 6e).
315
316 *Interaction of chromite nanoparticles with chamosite and organic matter*
317 One of the most prevalent interaction in the suspension containing chamosite particles is
318 the attachment of chromite, Cr-(hydr)oxide and altered hausmannite nanoparticles on surfaces of
319 the chamosite particles (experiments 3 and 4). For example, Figures 7a-e depict the attachment
320 of Cr-hydr(oxide)- and hausmannite nanoparticles on a highly altered chamosite particle, which

is partially covered by Fe-(hydr)oxide precipitates (bright areas in Fig. 7a and indicated with the corresponding Fe : Mg ratios in Fig. 7b). Attached cubic and needle-like Mn-oxide nanoparticles (hausmannite and manganite, Fig. S2) and Fe-(hydr)oxides precipitates are in close association whereas the Cr-(hydr)oxide nanoparticles seem randomly distributed over the surface of chamosite grain (Fig. 7a-d). High-resolution TEM studies and FFT-pattern indicate that parts of the attached Cr-(hydr)oxide nanoparticles are composed of grimaldiite (α-CrOOH) (Fig. 7d, e).

One of the most prevalent interactions in the suspension with the organic-rich soils (experiments 5 and 6) is the interaction between chromite nanoparticles and organic colloids. Figure 7f shows for example an organic colloid with two attached or incorporated aggregates of altered and unaltered chromite nanoparticle (labelled "1" and "2" in Fig. 7f). Aggregate 1 is composed of chemically unaltered nanoparticles of chromite (Fig. S9) whereas altered nanoparticles in aggregate 2 are enriched in Cr and Mn and depleted in Fe with respect to the synthesized chromite nanoparticles (Fig. 7f).

Chemical composition of the suspensions after 9 months of the long-term batch experiments

The pH values during all long-term batch experiments rose occasionally above pH = 5 and had to be re-adjusted mainly with a K-hydrogen phthalate solution (see above). The redox potential at this constant pH value varied only slightly in the range of Eh = 0.4 -0.43 V.

The Cr concentrations are in the μg kg^{-1} range (0.8-26.4 μkg^{-1}) and thus are much lower than the initial Cr concentration of 519.96 mg kg^{-1} in the leachate (Table 3 versus Table S2). The Fe concentrations are below the detection limit in most of the suspensions due to the higher detection limit for the element. The concentrations for Mn are variable across the six experiments with the lowest and highest concentrations in the suspensions with the chamosite

344 particles and organic-rich soils, respectively (Table 3). The concentrations of Cr^{3+} and Cr^{6+} in the
345 suspensions are below the detection limit of 1 μgkg^{-1} when analysed with the combination
346 chromatography/ICP-MS. The concentrations of Cr^{6+} in the suspensions are either below or
347 slightly above the detection limit of 0.5 μgL^{-1} when analysed with the combination of
348 chromatography/UV-VIS (Table 3). Here, the suspensions with the chamosite particles contain
349 the highest concentrations of Cr^{6+} with 4.0 and 4.1 $\mu g\ L^{-1}$ (Table 3).
350
351 **DISCUSSION**
352 We will address release of chromite nanoparticles in the leaching experiments before
353 discussing their interaction with hausmannite nanoparticles, clinochlore and organic matter at pH
354 = 5.
355
356 *Mineralogy of the colloidal fraction versus bulk dissolution data*
357 The chemical and mineralogical characterization of the silicate-enriched fraction after the
358 leaching experiments (Fig. 1a, Table 1) and the chemical composition of the leachates (Table 2)
359 suggest that
360 (a) small amounts of clinochlore dissolve at pH = 5 whereas the chromite grains remain
361 nearly unaltered (Fig. 4a);
362 (b) the differences in dissolution rates between clinochlore and chromite are smaller
363 under acidic than near neutral pH conditions; in accord with previous observations by
364 Schindler et al. (2018).
365 (c) the observed non-stochiometric dissolution of clinochlore (on the basis of the
366 chemical compositions of the solids and leachates, Table 1 and 2) may be the result of

367 the formation of Al-rich surface precipitates or larger Al-rich colloids which were
368 most likely filtered out prior to chemical analysis of the leachate (mesh size < 450
369 nm).

370 These observations agree with the TEM examinations of the colloidal fractions in both
371 leachates: (1) larger colloids of clinochlore (Fig. S5) and a Si-bearing Al-hydroxide in the
372 leachate of pH = 5 (Fig. 1a-d) indicate incomplete dissolution and non-stochiometric of
373 clinochlore, respectively; (2) many small Fe-, Cr- and Si-bearing colloids in the lower
374 nanometer size range (which were able to pass through the 450 nm filter) are present and absent
375 in the colloidal fractions of the leachates at pH = 2 and pH = 5, respectively (Fig. 1f).

376 Chromite nanoparticles were only identified in colloids composed of clinochlore (Fig.
377 S5) and on the surface of an amorphous Si-bearing Al-hydroxide in the leachate of pH = 5 (Fig.
378 1b and c, S6). The occurrence of attached and aggregated chromite nanoparticles on the surface
379 of the Al-hydroxide colloid indicates the presence of nanoparticles in the colloidal fraction of the
380 leachate of pH = 5. It seems unlikely that these nanoparticles originated from the breakdown of
381 micrometer-sized chromite grains as they (1) have similar sizes as those observed in clinochlore
382 and (2) contain only minor Mg (Fig. S6) whereas the micrometer-size chromite grains in the
383 chromitite sample have Fe : Mg ratios close to 1 : 1 (Table 1).

384

385 *Aggregation of nanoparticles and their attachment onto mineral surfaces*

386 The observed aggregation of chromite- and hausmannite- nanoparticles (Fig 2a-b) and
387 their attachment to larger chamosite and organic matter particles (Fig. 7) can be explained with
388 the Derjaguin-Landau-Verwey-Overbeak (DLVO) theory and extended Derjaguin-Landau-
389 Verwey-Overbeak (XDLVO) theory. According to these theories, pH and activity of dissolved

ions have a great influence on the surface charge and can either inhibit or promote aggregation. As the pH approaches the point of zero charge of a nanoparticle surface, electrostatic double layer repulsion decreases and aggregation is promoted by van der Waals attraction. Chromite and hausmannite have points of zero charge of around pHpzc = 6.0-6.5 and pHpzc = 5.7, respectively (Rousseau, 1987; Kosmulski, 2009) and their surfaces had thus slightly positive surface charges at pH = 5. This positive surface charge was neutralized in the suspension by the presence of negative counter ions such as phosphate and sulfate ions (Fig. 2a-b). These counter ions neutralised the slightly positive-charged EDL and van der Waals attractions became dominate and promoted the aggregation of the chromite and hausmannite nanoparticles (Fig. 2a-b).

Chlorite-group minerals have point of zero charges around pHpzc = 4-5 and thus their slightly-negative to neutral-charged surfaces at pH = 5 promoted the attachment of the positive-charged chromite and hausmannite nanoparticles (Fig 7a-e). The typical point of zero charge for organic matter in soils is pHpzc = 2 to 3 (Selinus and Alloway, 2005; Sparks, 2003) and the negative-charged surfaces of organic colloids at pH = 5 promoted also the attachment of the chromite nanoparticles (Fig. 7f).

Dissolution reprecipitation processes on the surface of hausmannite

The STEM/TEM studies indicate that the dissolution of chromite nanoparticles in the presence of hausmannite nanoparticle results in the formation of Cr- and Fe-hydroxide phases (Figs. 4-7). The corresponding dissolution-reprecipitation reactions are most likely catalysed by the oxidation of Fe^{2+} by Mn^{3+} species which is thermodynamically favoured over the oxidation of Mn^{2+} by Fe^{3+} species:

$$Mn^{3+} + Fe^{2+} \rightarrow Mn^{2+} + Fe^{3+} \qquad \Delta G°r = -103.14 \text{ kJ/mol} \qquad [1]$$

Or in terms of (hydr)oxides:

$$Mn_3O_4 + 2Fe^{2+} + 2H_2O \rightarrow 3Mn^{2+} + 2Fe(OH)_3 + H^+ \quad \Delta G°r = -61.36 \text{ kJ/mol} \qquad [2]$$

The resulting Fe^{3+} (hydr)oxides (equation [2]) form a porous surface layer or fillings within the hausmannite nanoparticles (Figs. 4-6 9), which allowed the continuous oxidation of Fe^{2+} to Fe^{3+}, the precipitation of Fe^{3+}-phases and the reductive dissolution of the Mn-oxide. This continuous dissolution-reprecipitation process has been also observed by others (Schaefer et al., 2017), and can eventually result in the pseudomorphic replacement of a Mn- by Fe-oxide mineral (Golden et al. 1988). Similarly, the attachment of Mn-oxide nanoparticles on the surface of the chamosite crystals resulted in the formation Fe^{3+}-(hydr)oxides most likely due to the oxidative dissolution of the underlying Fe^{2+}-bearing sheet silicate (Fig. 7a-c).

The mineralogical composition of the Fe-hydroxide rim on the surfaces of the hausmannite nanoparticles could not be unequivocally identified due to the absence of diffraction spots and lattice fringes. The precipitation of ferrihydrite seems however likely as it is commonly the first Fe-(hydr)oxide phase to precipitate from aqueous solution (Navrotsky et al. 2008; Guo and Barnard, 2013; Aeppli et al, 2019).

The formation of an Fe^{3+}-(hydr)oxide rim on the surface of hausmannite nanoparticles most likely impacts the overall ability of Mn oxides to remain redox-active phases in environmental systems. Experimental studies showed for example that the production of Mn^{2+} during equation [2] decreases with time, suggesting that the Fe^{3+} -hydroxide layers partially passivate $Mn^{3+/4+}$ terminations on the surface of Mn oxides (Villinski et al., 2001).

Large parts of the Cr-(hydr)oxides nanoparticles formed during the long-term batch experiment lack long-range (no diffraction spots in SAED pattern) (Fig. S8). The initial formation of an amorphous (or nanocrystalline) Cr-(hydr)oxide and its subsequent

436 transformation to the thermodynamically more stable phases bracewellite and grimaldiite (which
437 occur as nano-size crystals within the amorphous phase; Fig 6a-e, 7a-d) follows hereby
438 Ostwald's step rule.

439 There are three CrOOH polymorphs: α-CrOOH, grimaldiite, β-CrOOH, guyanaite and γ-
440 CrOOH, bracewellite. These phases are rare and only occur in a few locations with merumite, a
441 hydrated Cr-hydroxide ore discovered in Guyana, being the most prominent host of all three
442 phases (Bracewell, 1946; Milton et al. 1976). Similar to this study, Shpachenko et al. (2006)
443 identified bracewellite crystals grown in a matrix of an amorphous Cr-(hydr)oxide.

444

445 *Reaction pathways during the interaction of hausmannite and chromite nanoparticles*

446 The observations above clearly indicate the occurrence of dissolution-precipitation
447 processes involving dissolution of chromite and hausmannite and precipitation of Fe- and Cr-
448 hydroxides. These processes lead in some cases to the replacement of the Mn-oxide by a Fe-
449 (hydr)oxides (Figs. 4 and 5) and the replacement of chromite by Cr-hydr(oxides) (Fig. 6d-e).
450 They required the initial oxidation of Fe^{2+} to Fe^{3+} and reduction of Mn^{3+} to Mn^{2+}.

451 Using multichamber experiment with Cr^{3+}-Fe^{3+}-hydroxide being spatially separated from
452 Mn-oxides, Pan et al. (2019) showed that the reaction pathway $Cr^{3+} \rightarrow Cr^{6+}$ involves dissolution
453 of the Cr-bearing solid and transport of Cr^{3+} to the Mn-oxide surface and its subsequent
454 oxidation to Cr^{6+}.

455 The occurrence of Cr-rich Fe-(hydr)oxides (Figs.4 and 6-7) on the surface of the
456 hausmannite nanoparticles indicate that reduced Fe^{2+} and Cr^{3+} species occurred on the surfaces
457 of the hausmannite nanoparticles (some in form of attached chromite nanoparticles) and that a
458 (unknown) fraction of the Cr^{3+} reprecipitates with the Fe^{3+}-hydroxides during the reductive

459 dissolution of the Mn-oxide substrate (Fig. 3b). The presence of Mn in altered chromite
460 nanoparticles or Cr-(hydr)oxide precipitates (Fig. 3a and 6c) indicates the co-precipitation of Mn
461 species with Cr-(hydr)oxides during the oxidative dissolution of the chromite nanoparticles. It is
462 however unclear whether the oxidation of chromite was initiated by adsorbed Mn^{3+} species or
463 solid-solid interactions between hausmannite and chromite nanoparticles. A combination of
464 TEM, X-ray Photoelectron Spectroscopy and multichamber reaction cells will perhaps allow the
465 differentiation between oxidative dissolution processes involving adsorbed species versus solid-
466 solid interactions.
467
468 *The composition of the suspensions after the long-term experiments*
469 The observations above show complex solid-solid interactions such as dissolution,
470 reprecipitation, aggregation and attachment involving nanoparticles of chromite, hausmannite,
471 chamosite, organic matter, Fe- and Cr-(hydr)oxides and phosphate species. Hence, many factors
472 affected the concentrations of Cr (Cr^{3+} and Cr^{6+}), Fe and Mn in the leachate after the long-term
473 batch experiment. As such, we will point out here only major differences and similarities
474 between the different experiments.
475 The concentrations of Cr, Fe and Mn in the leachate and filtering (450 nm pore size) are
476 much lower (Table 3) than their initial concentrations (519.96 mg kg^{-1} , Table S2) and suggest
477 that the majority of Cr, Fe and Mn occur in aggregates with d > 450 nm. This conclusion is in
478 accord with the observed aggregates of chromite, hausmannite and chamosite particles (Figs. 2
479 and 4-7). However, the concentration of Cr and Mn in the leachates differ significantly between
480 the six experiments with the lowest and the highest concentrations of Cr and Mn in the leachates
481 with chamosite and organic rich soils, respectively (Table 3). The higher concentrations of Cr

and Mn in the solutions with organic matter can be either a result of (a) a lower degree of particle aggregation relative to the experiments without organic matter or (b) the enhanced complexation of Cr and Mn by dissolved organic matter (Dinu, 2013; Gustafsson et al., 2014). However, the latter scenario can be ruled out for Cr as the concentrations for Cr^{3+}aq and Cr^{6+}aq after their chromatographic separation from the chromite nanoparticles were below or close to the detection limits of the ICP-MS and UV-VIS (1 $\mu g kg^{-1}$ and 0.5 $\mu g kg^{-1}$).

As discussed above, pH and activity of dissolved ions have a great influence on the surface charge and can either inhibit or promote aggregation. As the pH was constant in all long-term batch experiments, the lower degree of particle aggregation in the suspension with organic matter may be explained with the presence of adsorbed dissolved organic matter (DOM) on the surfaces of the particles. Studies on the fate of natural colloids in the environment show that natural colloids with a wide range of chemical compositions are often negative-charged due to adsorbed DOM species (Philippe and Schaumann, 2014). These DOM species are mainly humic substances which either neutralize positive-charged surfaces and thus induce aggregation or cause electrosteric stabilization and hinder aggregation of the colloids (Philippe and Schaumann, 2014). Hence, humic substances adsorbed on the positive-charged surfaces of the hausmannite and chromite nanoparticles may have partially reversed their surface charges and subsequently lowered their degree of aggregation in the experiments with organic matter.

Two distinct analytical approaches (chromatography + ICP-MS versus chromatography + UV-VIS) indicated that the concentrations of Cr^{6+} in all suspensions after the long-term batch experiments were very low with the highest concentration around 4 $\mu g\ kg^{-1}$ (Table 3). These low concentrations of Cr^{6+} contradict previous observations on the oxidation of Cr^{3+} to Cr^{6+} in the presence of Mn^{3+} -bearing oxides such as hausmannite and birnessite (Weaver and Hochella,

505 2003, Oze et al. 2007, Pan et al. 2017, 2019). However, none of the previous studies were
506 conducted over a period of nine months and in the presence of reducing substances such as Fe^{2+}-
507 silicates and organic matter. Hence the observations in this study show that the formation and
508 occurrence of Cr^{6+} species in solutions can be limited in complex mineralogical and geochemical
509 systems, even in the presence of Mn^{3+}-oxides, due to the presence of adsorption sites on silicates,
510 organic matter, Fe- and Cr^{3+}-hydroxides. Future more simplified experimental studies need to be
511 carried to identify factors that either inhibit the formation of Cr^{6+} or sequester Cr^{6+} -species
512 formed during the oxidative dissolution of chromite nanoparticles.
513
514 **IMPLICATIONS**
515 The results of this study show that chromite nanoparticles persist through weathering of
516 their host silicates at pH = 5 and can be thus released into the environment. These observations
517 change our understanding of the potential risks of Cr-bearing silicates in mine tailings and soils.
518 The release of chromite nanoparticles as opposed to Cr^{3+}(aq) species has a large impact on the
519 fate of Cr in the environment as the behavior of nanoparticles is governed by surface reactions
520 and nanoparticle-nanoparticle interactions (Hochella et al., 2008).
521 This study gives for the first-time insight into mineralogical processes during the
522 interaction of chromite and Mn-oxides nanoparticles. Common mineralogical features are
523 1. the aggregation of chromite and hausmannite nanoparticles, which is (a) promoted
524 under near neutral pH conditions and the presence of adsorbed negative-charged
525 phosphate species and (b) partly inhibited by dissolved organic matter.
526 2. The dissolution of chromite and hausmannite nanoparticles and their (partial)
527 replacement by Cr- and Fe-hydroxides is facilitated by dissolution-reprecipitation

processes. The latter processes involve the redox-controlled dissolution of the parent phases chromite and Mn-oxides, their replacement by the daughter phases Fe- and Cr-hydroxides and the formation of porosity which allows a continuous mass exchange between the daughter-parent phases and the bulk solution.

Many experimental studies show that the oxidation of Cr^{3+} in species and solids occurs readily in the presence of Mn-oxides such as hausmannite and birnessite. This study shows, however, that elevated Cr^{6+} concentration may not necessarily form or occur after 9-months interaction of chromite and hausmannite nanoparticles if these particles are part of a complex mineralogical and geochemical system containing Cr^{6+}-reducing solids such as organic matter and Fe^{2+} silicates, precipitates of Fe- and Cr-hydroxides and inorganic and organic buffers.

ACKNOWLEDGEMENTS

This project was supported by the Best of Science award # ESSD-BIS201617-15 of the Ministry of the Environment, Conservation and Parks, Ontario, Canada to MS. We would like to thank Graeme Spiers for his continuous support of the project, Joy Gray Munroe and Pedro Jugo for their assistance with the synthesis of the chromite nanoparticles, M.B. McClenaghan for her comments of an earlier version of the MS, Abdul Khan at the Manitoba Institute of Materials for his assistance with the TEM studies and the MECP laboratories in Etobicoke and especially Teresa Switzer and Taddese Godeto for their assistance with the chemical analyses. We like to thank Associate Editor Fabrizio Nestola for handling the paper and two anonymous reviewers for their valuable comments on an earlier version of the paper.

552 **References**

553 Aeppli, M., Kaegi, R., Kretzschmar, R., Voegelin, A., Hofstetter, T. B., and Sander, M. (2019)
554 Electrochemical analysis of changes in iron oxide reducibility during abiotic ferrihydrite
555 transformation into goethite and magnetite, Environmental Science & Technology, 53,
556 3568-3578.

557 Aliofkhazraei, M., Ed. (2016) Handbook of nanoparticles, p.661-662. Springer, Switzerland.

558 Ball, J. W., and Izbicki, J. A. (2004) Occurrence of hexavalent chromium in ground water in the
559 western Mojave Desert, California. Applied Geochemistry, 19, 1123-1135.

560 Bracewell, S. (1946). The geology and mineral resources of British Guiana. Daily Chronicle,
561 Limited.

562 Cameron, M., and Papike, J. J. (1981) Structural and chemical variations in pyroxenes. American
563 Mineralogist, 66, 1-50.

564 Dinu, M. I. (2013) Metals complexation with humic acids in surface water of different natural–
565 climatic zones. EDP Sciences, 1, 32011.

566 Fandeur, D., Juillot, F., Morin, G., Olivi, L., Cognigni, A., Webb, S. M., Ambrosi, J., Fritsch, E.
567 Guyot, F., and Brown, Jr, G. E. (2009). XANES evidence for oxidation of Cr (III) to Cr (VI)
568 by Mn-oxides in a lateritic regolith developed on serpentinized ultramafic rocks of New
569 Caledonia. Environmental Science & Technology, 43, 7384-7390.

570 Fendorf, S.E., and Zasoski, R.J. (1992) Chromium(III) oxidation by delta-MnO_2. I.
571 Characterization. Environmental Science & Technology, 26, 79-85.

572 Griffiths, N.A., Sebestyen, S.D. and Oleheiser, K.C. (2019) Variation in peatland porewater
573 chemistry over time and space along a bog to fen gradient. Science of the Total
574 Environment 697, 134152-134165.

Godgul, G., and Sahu, K.C. (1995) Chromium contamination from chromite mine. Environmental Geology, 25, 251-257.

Golden, D. C., Chen, C. C., Dixon, J. B., and Tokashiki, Y. (1988) Pseudomorphic replacement of manganese oxides by iron oxide minerals. Geoderma, 42, 199-211.

Guo, H., and Barnard, A. S. (2013) Naturally occurring iron oxide nanoparticles: morphology, surface chemistry and environmental stability. Journal of Materials Chemistry A, 1, 27-42.

Gustafsson, J. P., Persson, I., Oromieh, A. G., van Schaik, J. W., Sjös edt, C., and Kleja, D. B. (2014) Chromium (III) complexation to natural organic matter: mechanisms and modeling. Environmental Science & Technology, 48, 1753-1761.

Hausladen, D. M., and Fendorf, S. (2017) Hexavalent chromium generation within naturally structured soils and sediments. Environmental Science & Technology, 51, 2058-2067.

Hochella, M.F., Lower, K.S., Maurice, P.A., Penn, R.L., Sahai, N., Sparks, D.L., Twining, B.S. (2008) Nanominerals, mineral nanoparticles, and earths systems. Science, 319, 1631-1635.

Hotze, E. M., Phenrat, T., and Lowry, G. V. (2010) Nanoparticle aggregation: challenges to understanding transport and reactivity in the environment. Journal of Environmental Quality, 39, 1909-1924.

Huebner, J. S., Lipin, B. R., and Wiggins, L. B. (1976) Partitioning of chromium between silicate crystals and melts. Lunar and Planetary Science Conference Proceedings. 7, 1195-1220.

Jiang, W., Cai, Q., Xu, W., Yang, M., Cai, Y., Dionysiou, D.D., and O'Shea, K.E. (2014) Cr (VI) adsorption and reduction by humic acid coated on magnetite. Environmental Science & Technology, 48, 8078-8085.

Kaptay, G. (2012) On the size and shape dependence of the solubility of nano-particles in solutions. International Journal of Pharmaceutics, 430, 253-257.

598 Kosmulski, M. (2009) Surface charging and points of zero charge (Vol. 145), 334 p. CRC press.
599 Kumar, R., Rawat, K.S., and Mishra, A.K. (2012) Nanoparticles in the soil environment and their
600 behaviour: An overview. Journal of Applied and Natural Science, 4, 310-324.
601 Laarman, J.E. (2013) Detailed metallogenic study of the McFaulds lake chromite deposits,
602 Northern Ontario. Ph.D. thesis, The University of Western Ontario, pp. 494,
603 Manning, A. H., Mills, C. T., Morrison, J. M., and Ball, L. B. (2015) Insights into controls on
604 hexavalent chromium in groundwater provided by environmental tracers, Sacramento
605 Valley, California, USA. Applied Geochemistry, 62, 186-199.
606 Mével, C., & Kienast, J. R. (1986) Jadeite-kosmochlor solid solution and chromian sodic
607 amphiboles in jadeitites and associated rocks from Tawmaw (Burma). Bulletin de
608 Minéralogie, 109, 617-633.
609 Milton, C., Appleman, D. E., Appleman, M. H., Chao, E.C., Cuttitta, F., Dinnin, J.I., Dwornik,
610 E.J., Ingram, B.L., and Rose, H.J. (1976) Merumite- a Complex Assemblage of Chromium
611 Minerals from Gayana. U.S. geological survey, Prof. Paper 887, 1–29
612 Morrison, J. M., Goldhaber, M. B., Mills, C. T., Breit, G. N., Hooper, R. L., Holloway, J. M.,
613 Diehl, S.F., and Ranville, J. F. (2015) Weathering and transport of chromium and nickel
614 from serpentinite in the Coast Range ophiolite to the Sacramento Valley, California,
615 USA. Applied Geochemistry, 61, 72-86.
616 Navrotsky, A., Mazeina, L., and Majzlan, J. (2008). Size-driven structural and thermodynamic
617 complexity in iron oxides. Science, 319, 1635-1638.
618 Pan, C., Liu, H., Catalano, J.G., Qian, A., Wang, Z., Giammar, D.E. (2017) Rates of Cr(VI) Generation
619 from $Cr_xFe_{1-x}(OH)_3$ Solids upon Reaction with Manganese Oxide. Environmental Science &
620 Technology 51, 12416-12423.

621 Pan, C., Liu, H., Catalano, J.G., Wang, Z., Qian, A., Giammar, D.E. (2019) Understanding the
622 Roles of Dissolution and Diffusion in $Cr(OH)_3$ Oxidation by δ-MnO_2 *ACS Earth Space*
623 *Chemistry* 3, 357–365.Oliveira, H. (2012) Chromium as an environmental pollutant:
624 insights on induced plant toxicity. Journal of Botany, vol. 2012.
625 Oze, C., Fendorf, S., Bird, D.K., and Coleman R.G. (2004) Chromium geochemistry in
626 serpentinized ultramafic rocks and serpentine soils from the Franciscan complex of
627 California. American Journal of Science, 304, 67-101.
628 Oze, C., Bird, D. K., and Fendorf, S. (2007) Genesis of hexavalent chromium from natural
629 sources in soil and groundwater. Proceedings of the National Academy of Sciences, 104,
630 6544-6549.
631 Philippe, A., and Schaumann, G. E. (2014) Interactions of dissolved organic matter with natural
632 and engineered inorganic colloids: a review. Environmental Science & Technology, 48,
633 8946-8962.
634 Phillips, T. L., Loveless, J. K., and Bailey, S. W. (1980). Cr^{3+} coordination in chlorites: a
635 structural study of ten chromian chlorites. American Mineralogist, 65, 112-122.
636 Platonov, A. N., Langer, K., Andrut, M., and Calas, G. (1996). Cr^{3+} in phyllosilicates: influence
637 of the nature of coordinating ligands and their next cationic neighbors on the crystal field
638 parameters. The Geochemical Society Special Publication, 5, 41-48.
639 Robles-Camacho, J., and Armienta, M. A. (2000) Natural chromium contamination of
640 groundwater at Leon Valley, Mexico. Journal of Geochemical Exploration, 68, 167-181.
641 Rousseau, R. W., Ed. (1987). Handbook of Separation Process Technology. John Wiley & Sons.

642 Roy, D. M., and Roy, R. (1954). An experimental study of the formation and properties of
643 synthetic serpentines and related layer silicate minerals. American Mineralogist, 39, 957-
644 975.
645 Schaefer, M. V., Handler, R. M., and Scherer, M. M. (2017) Fe (II) reduction of pyrolusite (β-
646 MnO_2) and secondary mineral evolution. Geochemical transactions, 18, 7-18.
647 Schindler, M., Berti, D., and Hochella, M. F. (2017). Previously unknown mineral-nanomineral
648 relationships with important environmental consequences: The case of chromium release
649 from dissolving silicate minerals. American Mineralogist, 102, 2142-2145.
650 Schindler, M., Lussier, A. J., Principe, E., and Mykytczuk, N. (2018) Dissolution mechanisms of
651 chromitite: Understanding the release and fate of chromium in the environment. American
652 Mineralogist, 103, 271-283.
653 Selinus O., and Alloway B. J. (2005) Essentials of Medical Geology: Impacts of the Natural
654 Environment on Public Health, Elsevier Academic Press.
655 Shpachenko, A. K., Sorokhtina, N. V., Chukanov, N. V., Gorshkov, A. N., and Sivtsov, A. V.
656 (2006) Genesis and compositional characteristics of natural γ-CrOOH. Geochemistry
657 International, 44, 681-689.
658 Smith, C. A. S., Webb, K. T., Kenney, E., Anderson, A., and Kroetsch, D. (2011) Brunisolic
659 soils of Canada: Genesis, distribution, and classification. Canadian Journal of Soil
660 Science, 91, 695-717.
661 Sparks, D. L. (2003) Environmental soil chemistry, 2nd ed., Elsevier Science & Technology
662 Books.
663 Theng, B.K., and Yuan, G. (2008) Nanoparticles in the soil environment. Elements, 4, 395-399.

664 Villinski, J. E., O'Day, P. A., Corley, T. L., and Conklin, M. H. (2001) In situ spectroscopic and
665 solution analyses of the reductive dissolution of MnO2 by Fe (II). Environmental Science &
666 Technology, 35, 1157-1163.
667 Weaver, R.M., and Hochella, M.F. (2003) The reactivity of seven Mn-oxides with Cr^{3+}aq: A
668 comparative analysis of a complex, environmentally important redox reaction. American
669 Mineralogist, 88, 2016-2027

670

671

672 **FIGURE CAPTIONS**

673 **FIGURE 1.** (a) SEM-BSE image of an etched clinochlore grain (chl) after leaching of a silicate-
674 enriched chromitite powder with a solution of pH = 5; (b) STEM and (c) STEM-EDS chemical
675 distribution maps for Cr (green), Fe (red) of an Al-rich colloid deposited from the leachate of pH
676 = 5 on the carbon lath of the TEM holder; (d) high resolution TEM image of the chromite
677 nanoparticles on the surface of the Al-rich colloid (indicated with a rectangle in b) with
678 characteristic lattice fringes of chromite with d-spacings of 2.1 Å (400) and 2.9 Å (220); (e)
679 STEM and (c) STEM-EDS chemical distribution maps for Cr (green), Fe (red) and Si (yellow) of
680 many small Fe-, Cr- and Si-rich colloids in the leachate of pH = 2,

681

682 **FIGURE 2.** (a) STEM image and b) STEM-EDS chemical distribution map for Cr (green), Mn
683 (blue) and P (red) of an aggregate of hausmannite (Hsm), chromite (Chr) and manganite
684 nanoparticles in a suspension without chamosite and organic matter.

685

686 **FIGURE 3.** Chemical composition of chromite, hausmannite nanoparticles and chamosite
687 particles after the long-term experiments: Ternary plots depicting (a)-(b) Cr : Mn : Fe ratios in (a)

688 altered chromite nanoparticles (blue) in comparison to the ideal stoichiometry of an unaltered
689 chromite (red); (b) altered hausmannite nanoparticles; (c) the Al : Mg : Fe ratio in altered
690 chamosite grains (black) in comparison to the ideal stoichiometry of an unaltered chamosite
691 (red).
692
693 **FIGURE 4.** (a) STEM image and (b)-(d) STEM-EDS chemical maps for (b) Fe (red) and Cr
694 (green), (c) Fe (red) and Mn (blue) and (d) Mn (blue) and Si (yellow) of an aggregate containing
695 two hausmannite (Hsm) and the remains of a chromite (Chr) nanoparticle.
696
697 **FIGURE 5.** (a) STEM image of an aggregate of hausmannite (Hsm) and chromite (chr)
698 nanoparticles, the area shown in (b)-(d) is indicated with a rectangle; (b) STEM image (c)
699 STEM-EDS chemical map for Fe (red), Cr(green) and Mn (blue) and (d) high resolution TEM
700 image of the area depicted in (b); etch features and a rim of a Fe-(hydr)oxide are indicated with
701 arrows.
702
703 **FIGURE 6.** (a) TEM image and (b)-(c) STEM-EDS chemical maps for (b) Fe (red) and Cr
704 (green) and (c) Fe (red) and Mn (blue) of an aggregate of chromite nanoparticles (chr) with an
705 Cr-(hydr)oxide precipitate containing two parallel rods of bracewellite rods (γ-CrO(OH)); (d)
706 STEM image and (e) STEM-EDS chemical distribution map for Fe (red), Cr (green), Mn (blue),
707 Si (yellow) of an aggregate containing hausmannite nanoparticles (hsm), an unidentified clay
708 mineral and the remains of a chromite nanoparticle with two rods of bracewellite (γ-CrO(OH));
709 the area shown in (f) is indicated with a rectangle in (e); (f) TEM image of two rods of
710 bracewellite.

711 **FIGURE 7**. (a) STEM image and (b) STEM-EDS chemical map for Fe (green), Cr (red) and Mn
712 (pink) of a chamosite grain from with attached Cr-(hydr)oxides and hausmannite nanoparticles;
713 the areas shown in (c) and (d-e) are indicated with rectangles in (b); (c) STEM image of
714 hausmannite nanoparticles attached to the chamosite grain; (d) TEM image and (e) high-
715 resolution TEM image of a Cr-(hydr)oxide grain attached to a chamosite grain, the area shown in
716 (e) is indicated with a rectangle in (d); a FFT pattern (inlet) indicates that the lattice fringes in (e)
717 have characteristic d-spacings of grimaldiite (α-CrO(OH)); (f) STEM image of chromite
718 nanoparticle aggregates (chr) attached to a larger organic matter colloid (OM); aggregate 1 is
719 composed of weakly-altered chromite nanoparticles whereas aggregate 2 is highly altered and is
720 depleted in Fe and enriched in Mn relative to aggregate 1 (see supplementary data).
721
722
723
724
725
726
727
728
729
730
731
732
733

TABLE 1. Chemical composition of chromitite (Chr) and a silicate-enriched fraction (Sef) from the Black Thor deposit in weight% [wt%] and as atomic ratios relative to Si with *M* = Al, Cr, Fe and Mg

Oxide	Chr wt%	*M*/Si	Sef wt%	*M*/Si
Al_2O_3	13.52	4.4	12.74	1
Cr_2O_3	46.69	10.3	28.45	1.5
Fe_2O_3	21.27	4.5	13.88	0.7
MgO	12.89	5.3	23.13	2.3
SiO_2	3.64	---	15.4	

Average compositions of chromite and clinchlore are: $(Fe_{0.5}Mg_{0.5})(Al_{0.6}Cr_{1.4})O_4$ and $Mg_3[Si_4O_{10}(OH)_2]$ x $(MgAl_{1.33}(OH)_6)$, respectively. Clinochlore contains 3 at% Cr (Schindler et al. 2017, 2018).

TABLE 2. Chemical composition of the solution after leaching of the silicate-enriched fraction of chromitite at pH = 2 and 5 in [μg kg^{-1}] and as atomic ratios relative to Si with *M* = Al, Cr, Fe and Mg

	pH = 2 (n = 3)	*M*/Si	pH = 5 (n = 4)	M/Si
Al	3281	0.6	8	0.02
Cr	1059	0.1	6	0.01
Fe	2682	0.23	B.D.L.	---
Mg	8426	1.7	1322	4.25
Si	5756	---	360	---

765 **TABLE 3**. Chromium-, Fe- and Mn- concentrations in the suspensions (pH = 5) after the 9
766 months batch experiments (detection limits for Cr, Cr^{6+}, Fe, Mn = 0.2, 0.5, 50 and 1.0 [μgkg^{-1}]);
767 the solutions were filtered (450 nm filer) but not centrifuged; Cr = chromite nanoparticles, Mn =
768 hausmannite nanoparticles, Si = 10 gr chamosite, or = 10 gr organic rich soil; bdl = below
769 detection limit

Experiment	**Eh [V]**	**Cr [$mgkg^{-1}$]**	**Cr^{6+} [μgkg^{-1}]**	**Fe [$mgkg^{-1}$]**	**Mn [$mgkg^{-1}$]**	**P [$mgkg^{-1}$]**
1: Cr-Mn = 1 : 1	0.43	0.0200	0.6	Bdl	19.11	2.903
2: Cr-Mn = 1 : 5	0.40	0.0028	<0.5	Bdl	15.66	4.681
3: Cr-Mn = 1 : 1, Si	0.41	0.0008	4.0	0.07	8.74	0.157
4: Cr-Mn = 1 : 5, Si	0.41	0.0014	4.1	Bdl	7.57	3.321
5: Cr-Mn = 1 : 1, Or	0.42	0.0300	0.6	0.01	25.40	0.125
6: Cr-Mn = 1 : 5, Or	0.43	0.0264	0.9	Bdl	38.32	0.040

770

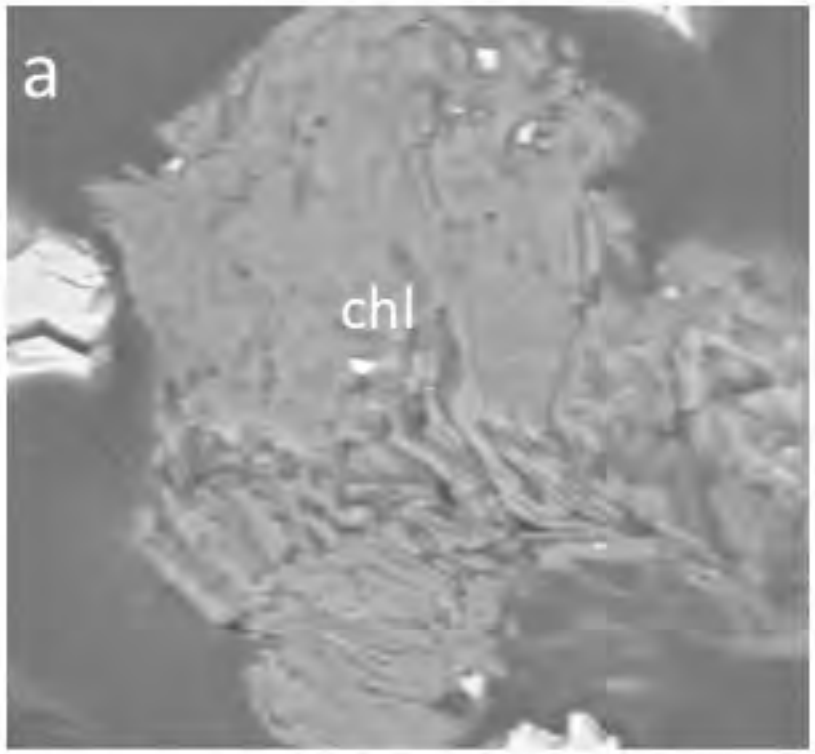
a
chl
60µm

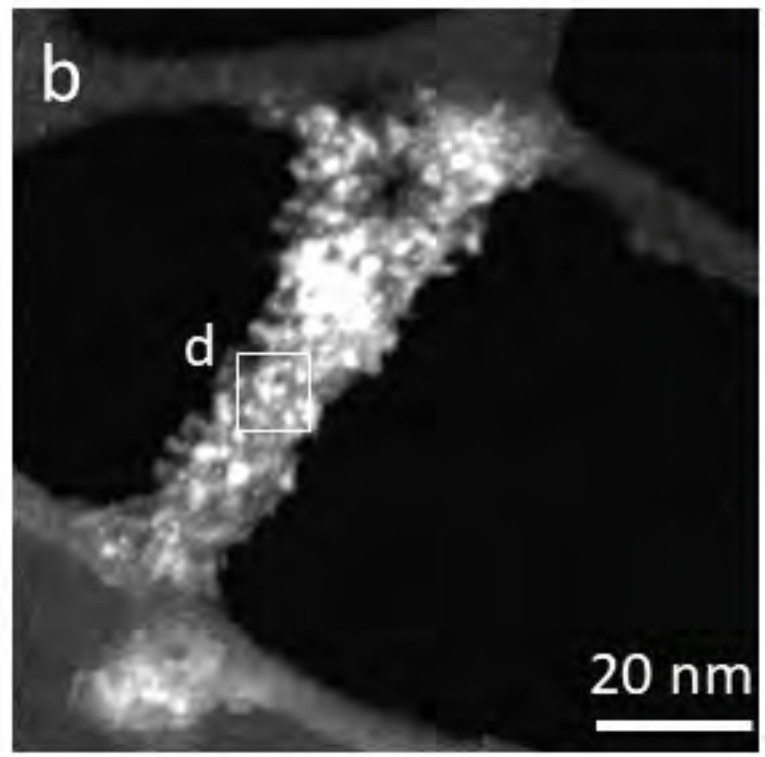
b
d
20 nm

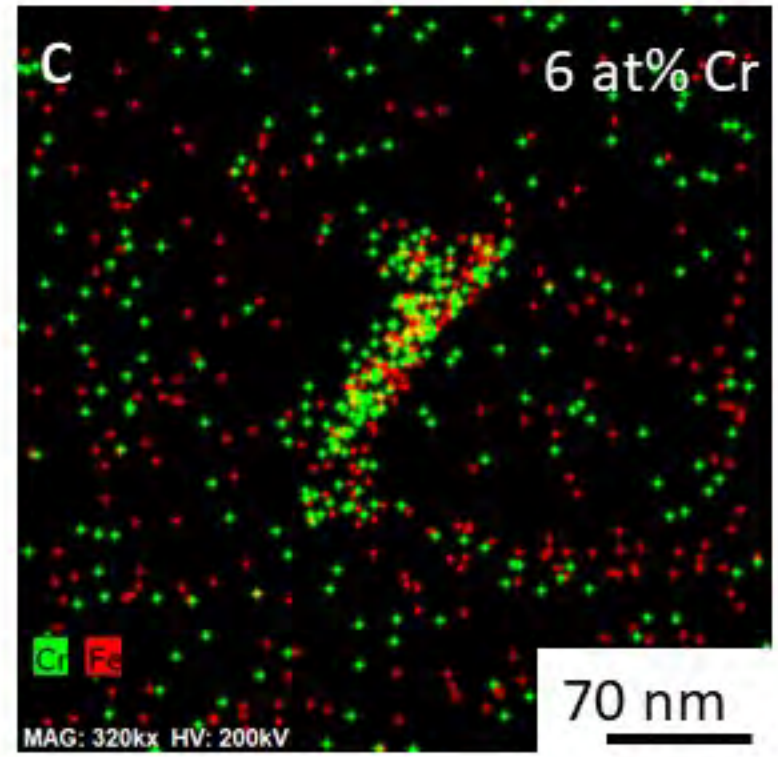
c
6 at% Cr
Cr
Fe
MAG: 320kx HV: 200kV
70 nm

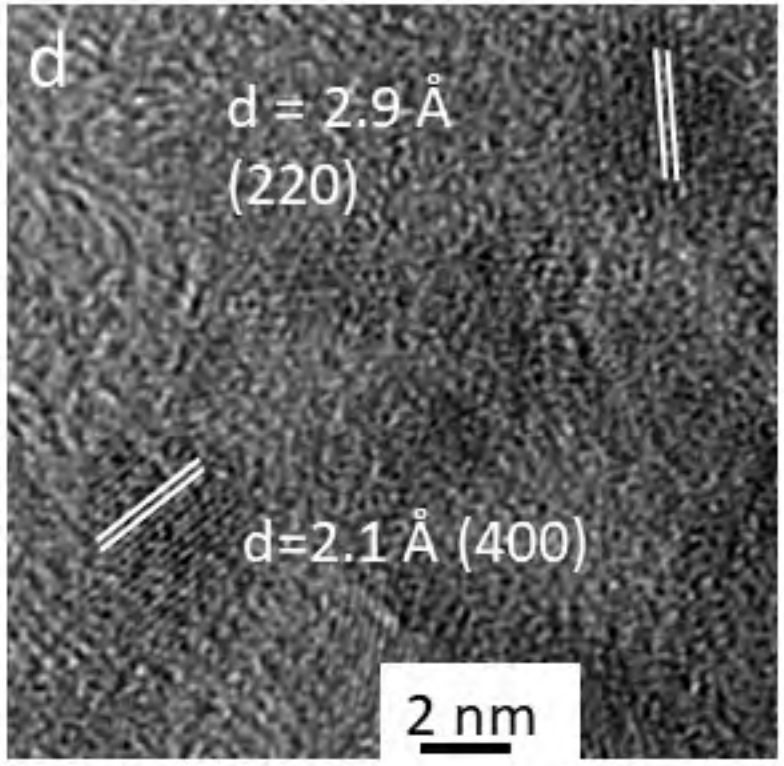
d
d = 2.9 Å
(220)
d=2.1 Å (400)
2 nm

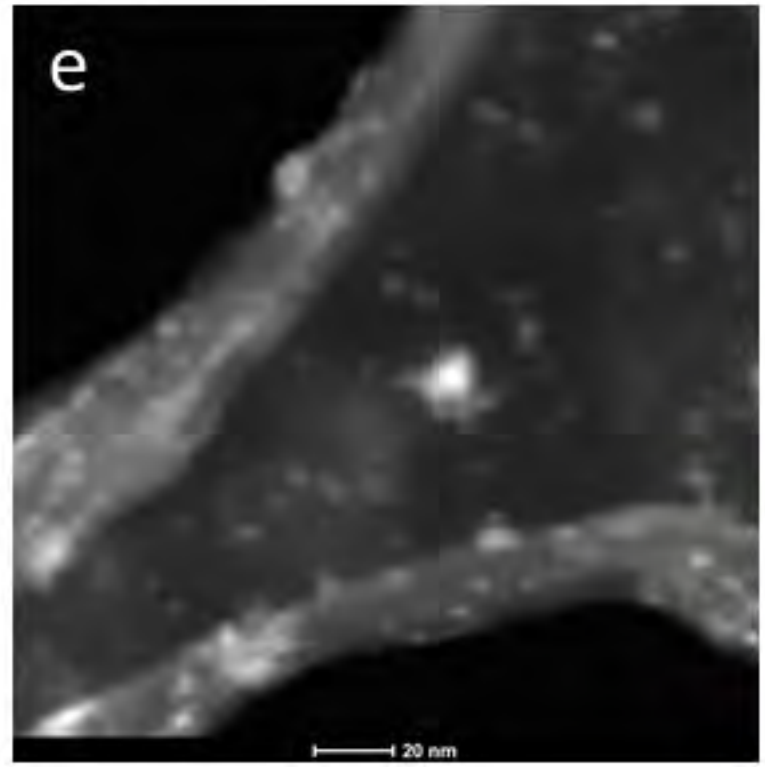
e
20 nm

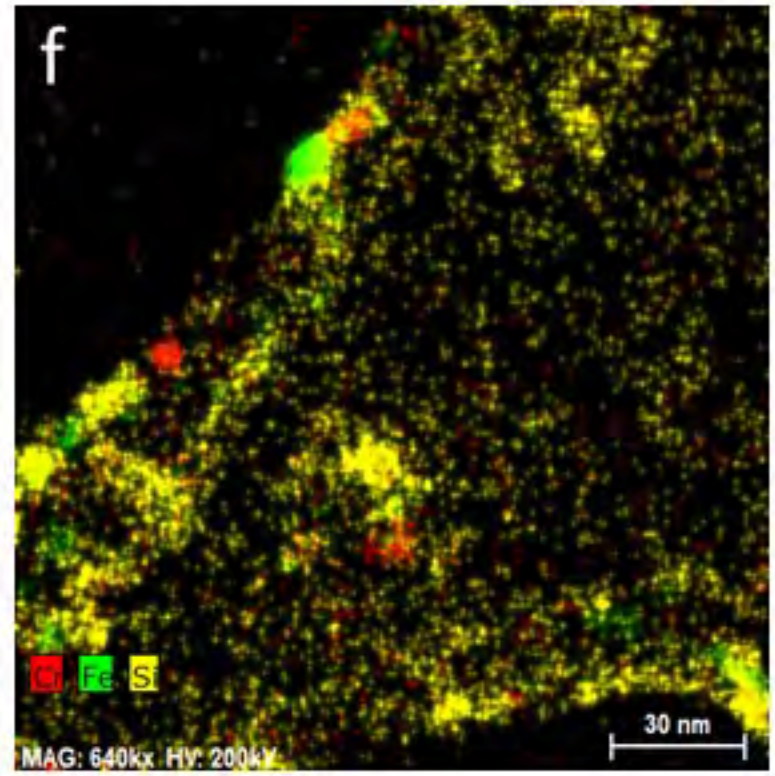
f
Cr
Fe
Si
MAG: 640kx HV: 200kV
30 nm

Figure 1

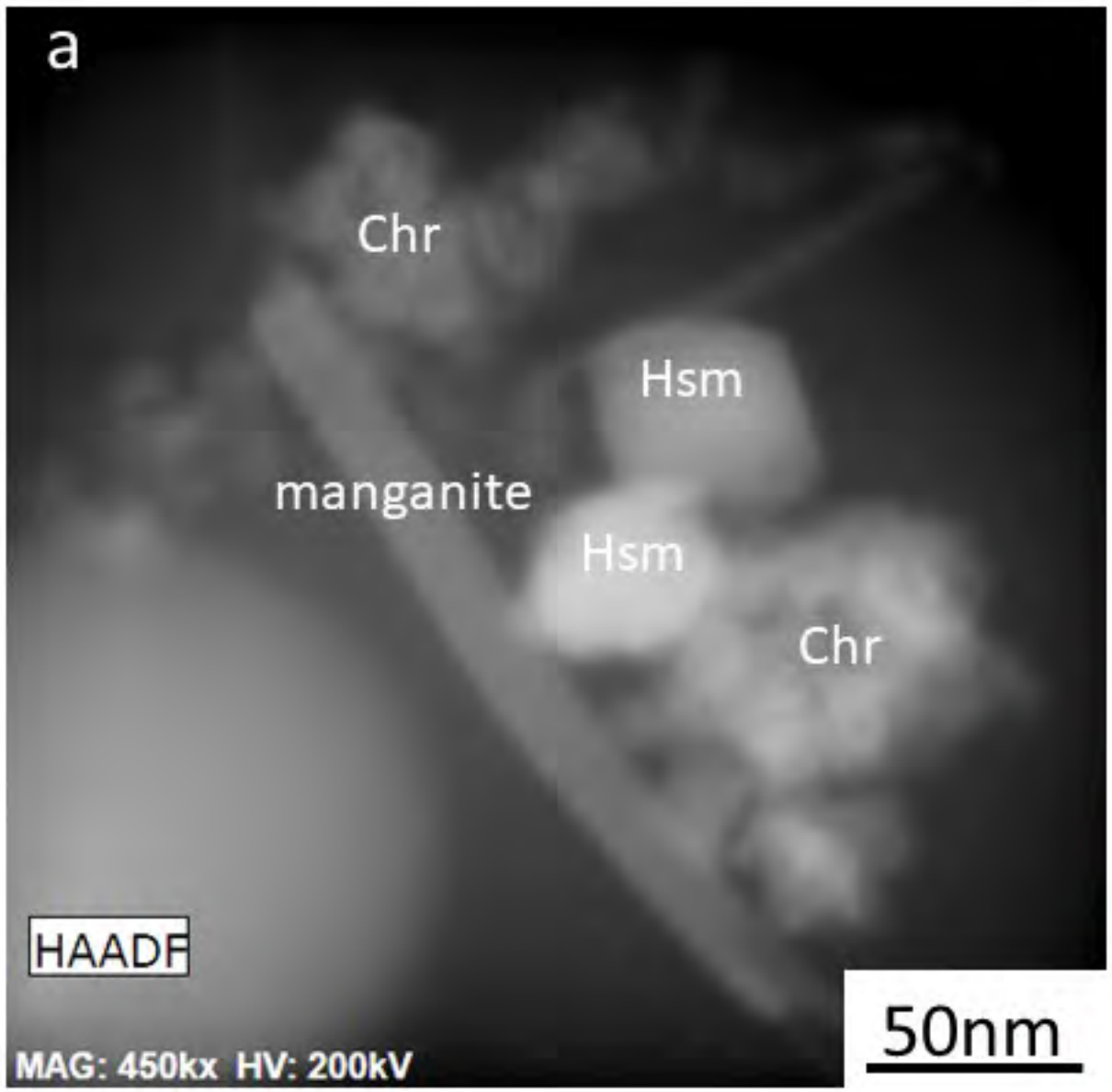
a
Chr
Hsm
manganite
Hsm
Chr
HAADF
MAG: 450kx HV: 200kV
50nm

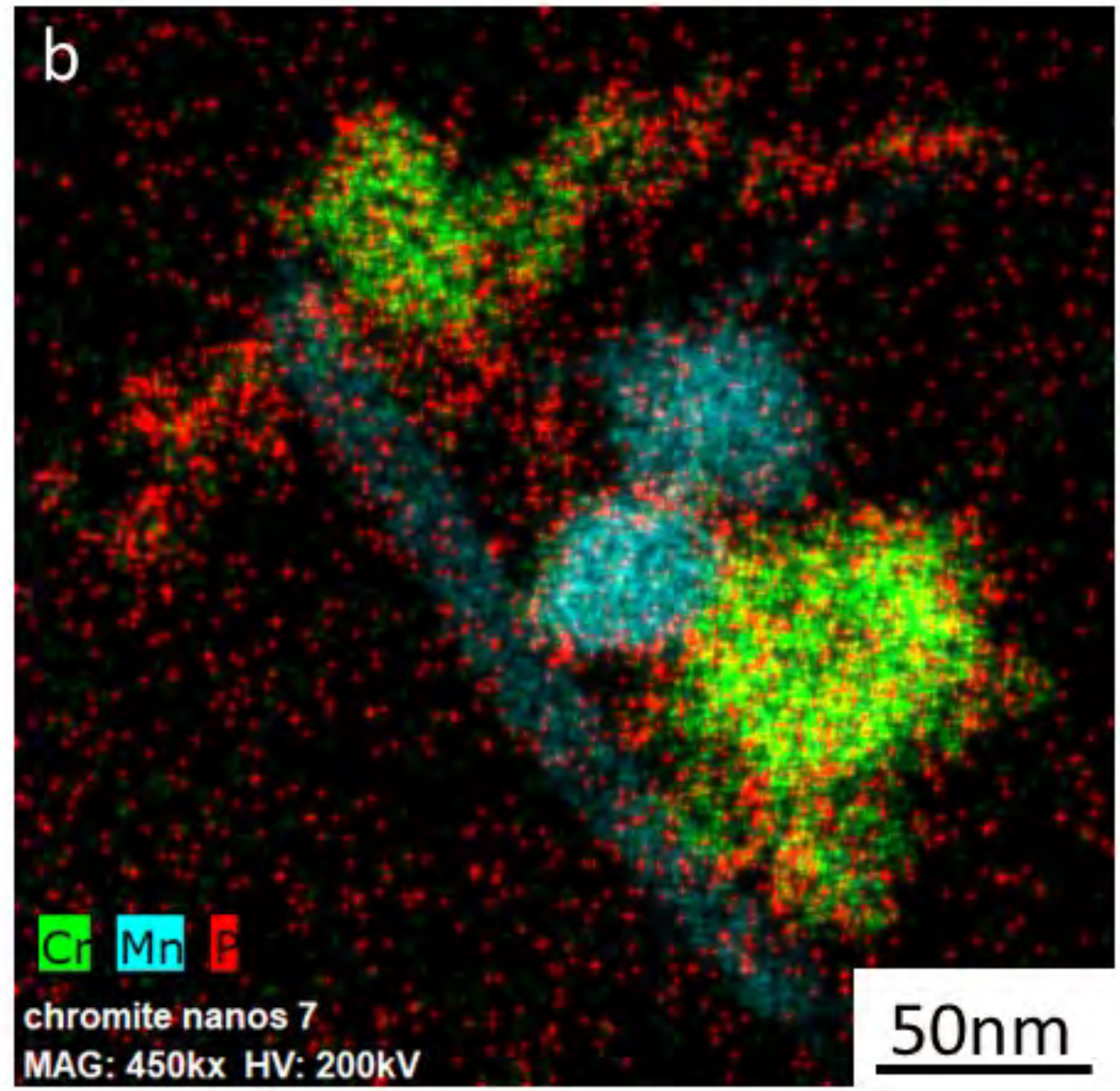
b
Cr
Mn
Fe
chromite nanos 7
MAG: 450kx HV: 200kV
50nm

Figure 2

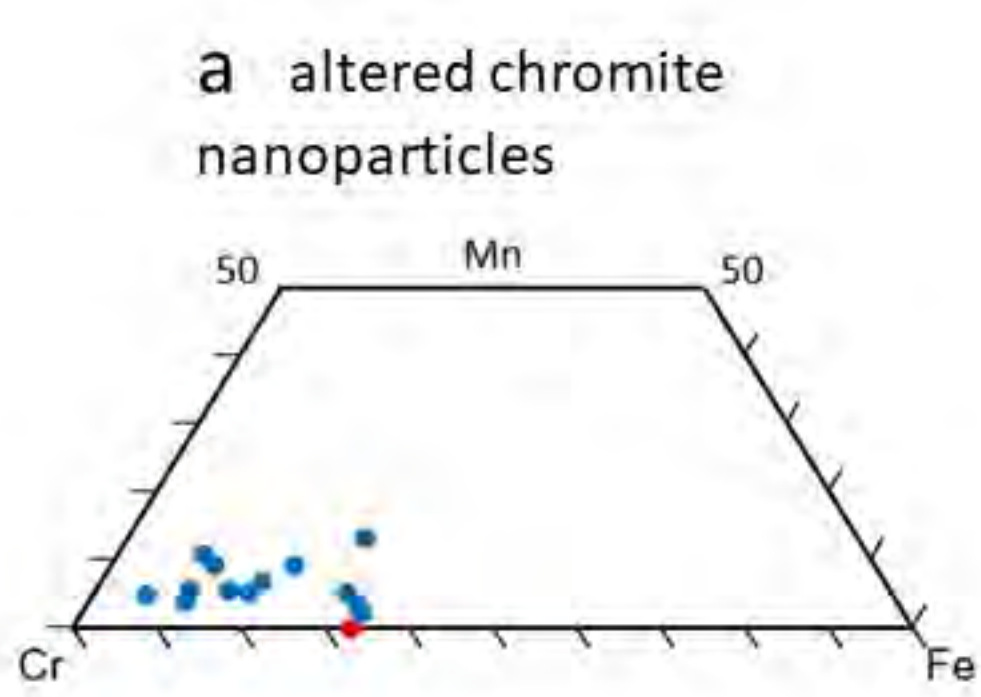
a altered chromite nanoparticles
50
Mn
50
Cr
Fe

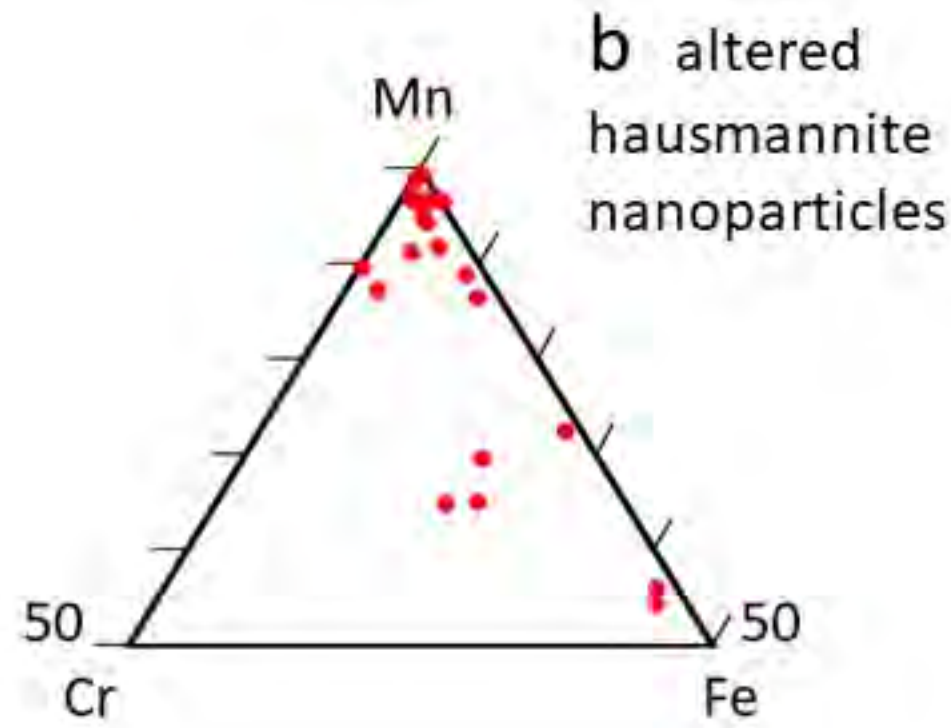
b altered hausmannite nanoparticles
Mn
50
Cr
50
Fe

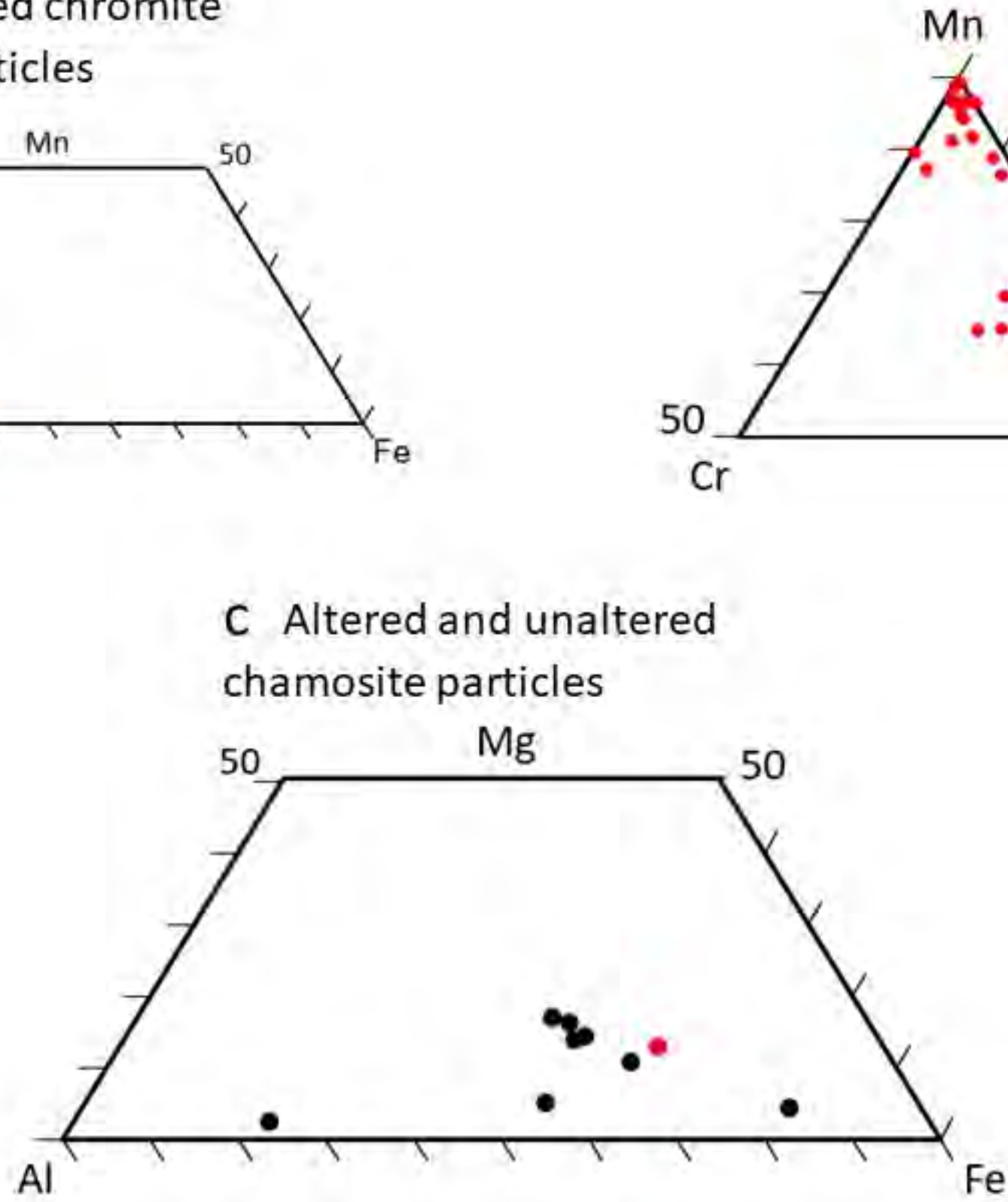
C Altered and unaltered chamosite particles
50
Mg
50
Al
Fe

Figure 3

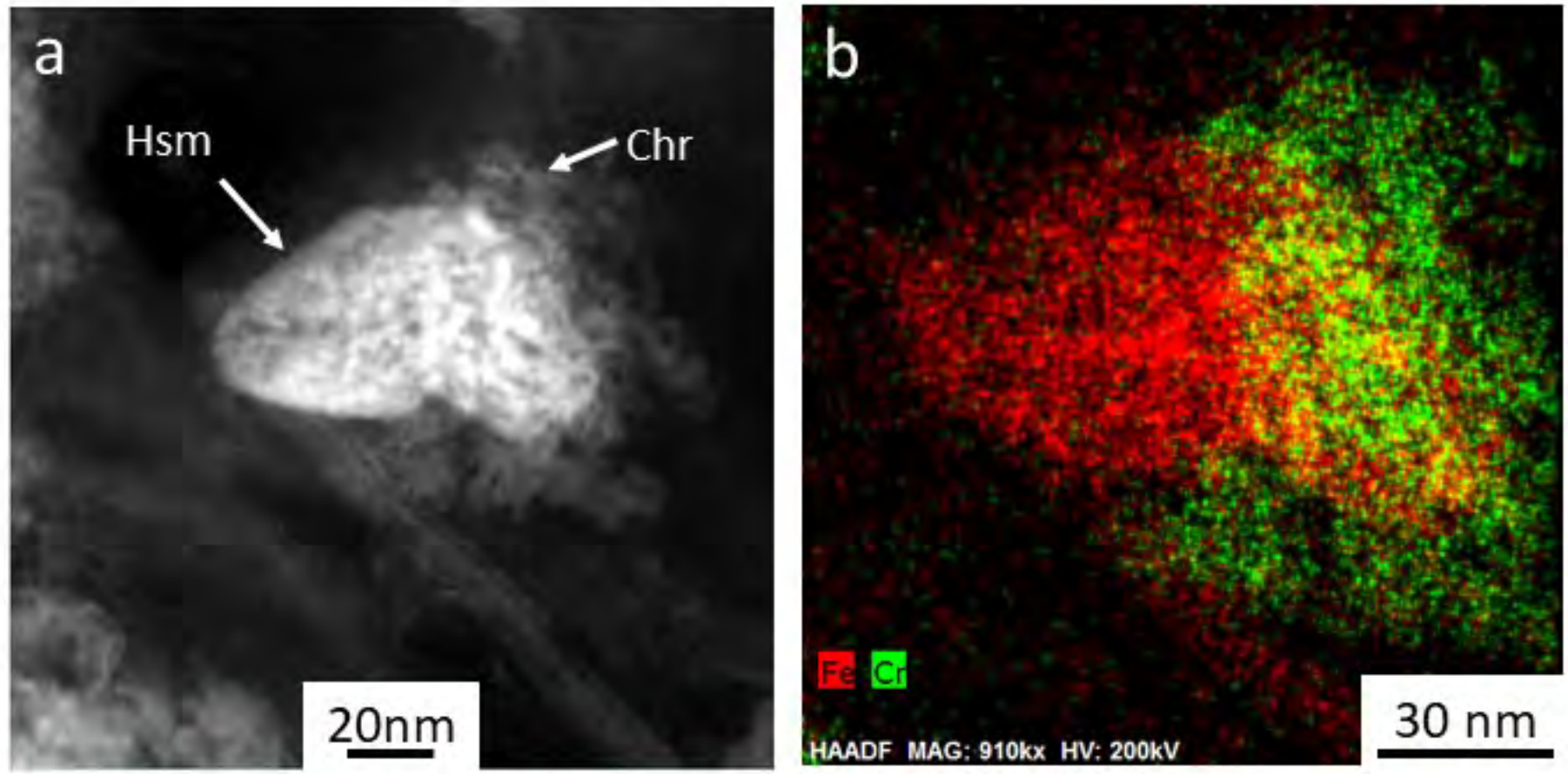
a
Hsm
Chr
20nm
b
Fe Cr
HAADF MAG: 910kx HV: 200kV
30 nm
c
Fe Mn
HAADF MAG: 910kx HV: 200kV
30nm
d
Mn Si
MAG: 910kx HV: 200kV
30nm

Figure 4

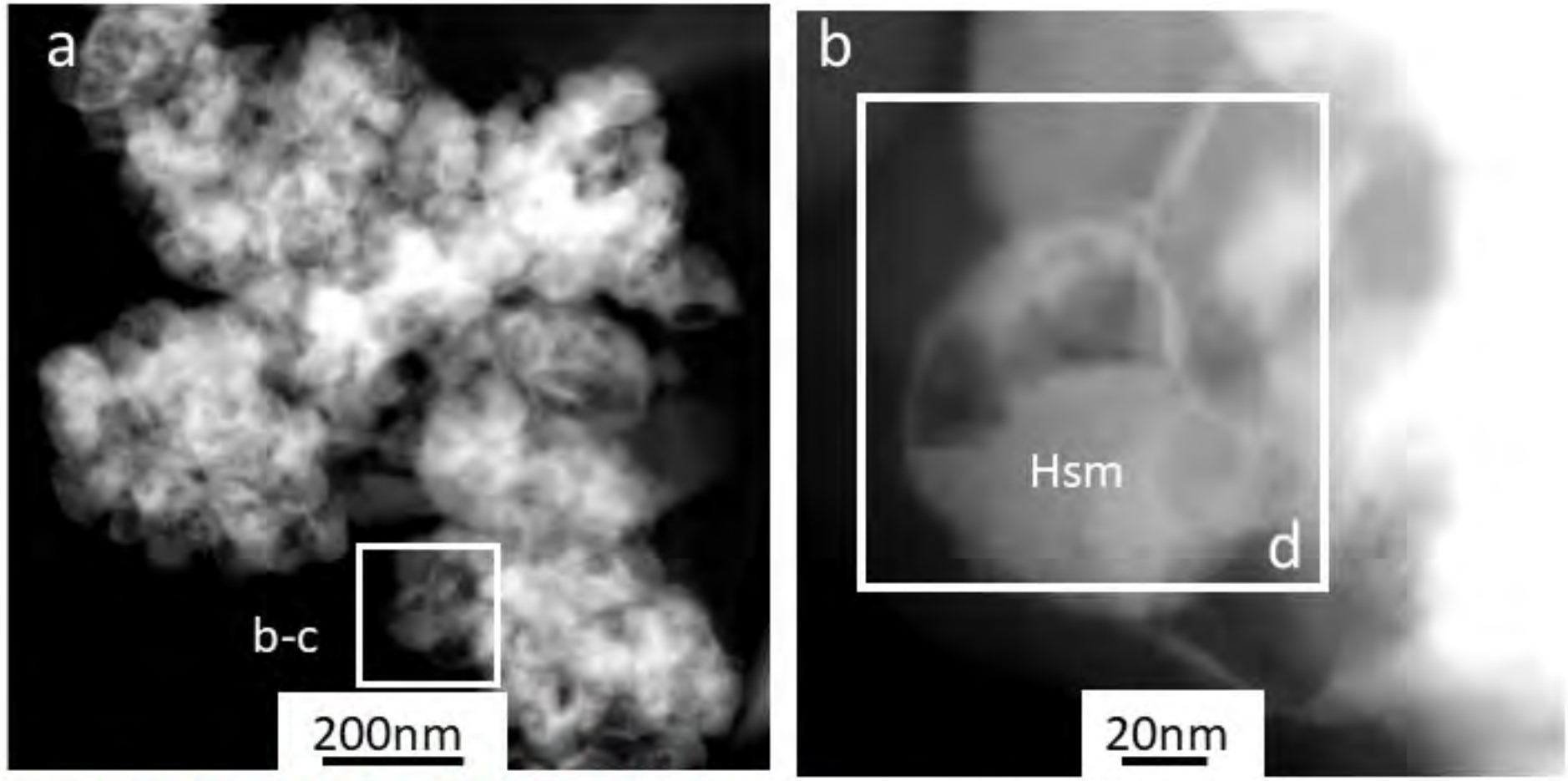
a
b-c
200nm
b
Hsm
d
20nm
c
FeOx
Fe
Cr
Mn
MAG: 640kx HV: 200kV
chr
30nm
d
FeOx
Etch
features
20nm

Figure 5

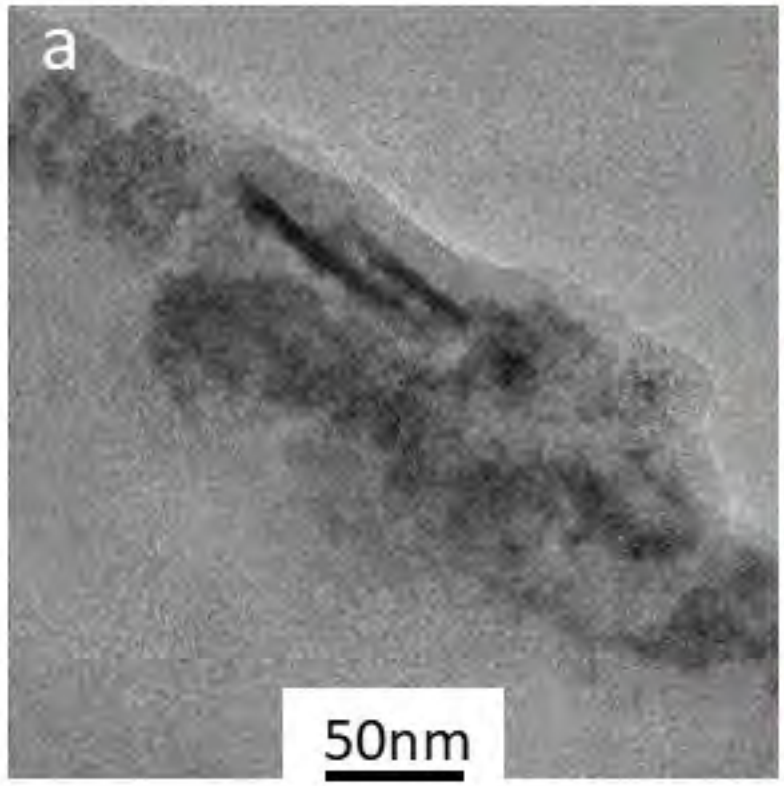
a
50nm

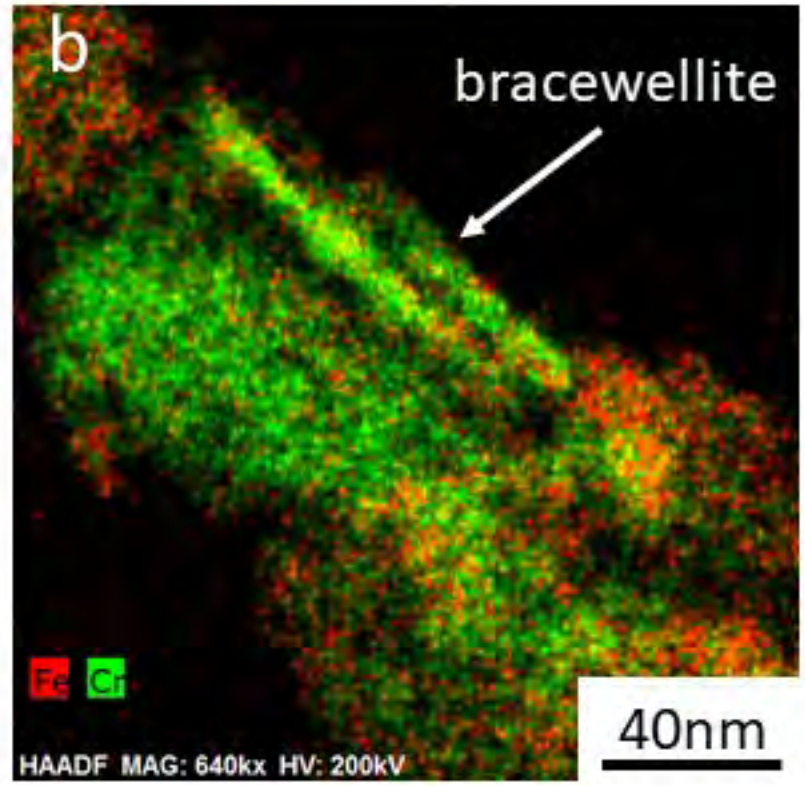
b
bracewellite
Fe Cr
HAADF MAG: 640kx HV: 200kV
40nm

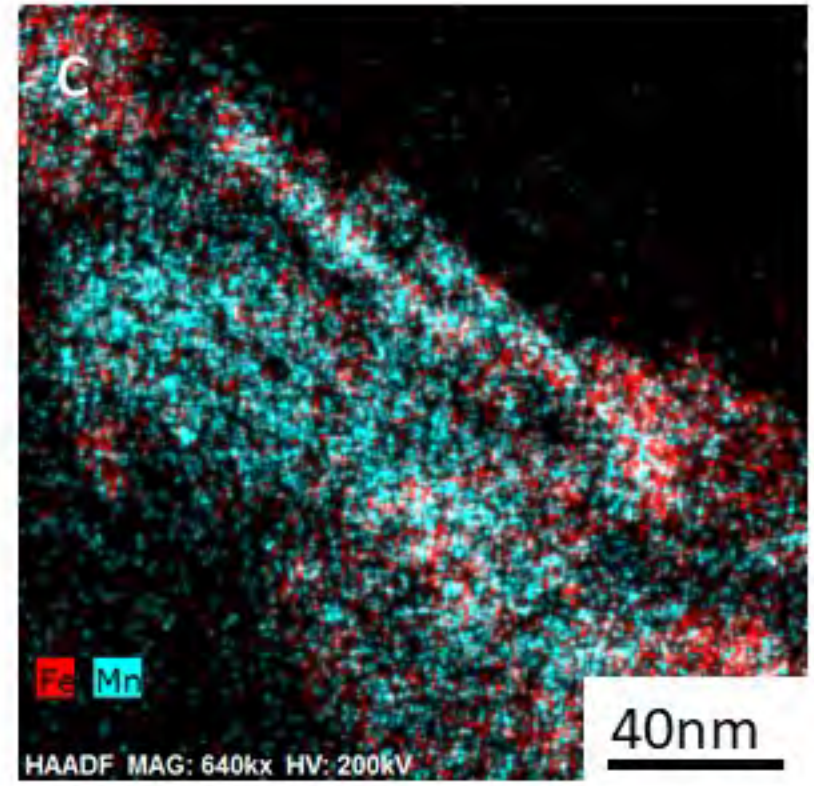
c
Fe Mn
HAADF MAG: 640kx HV: 200kV
40nm

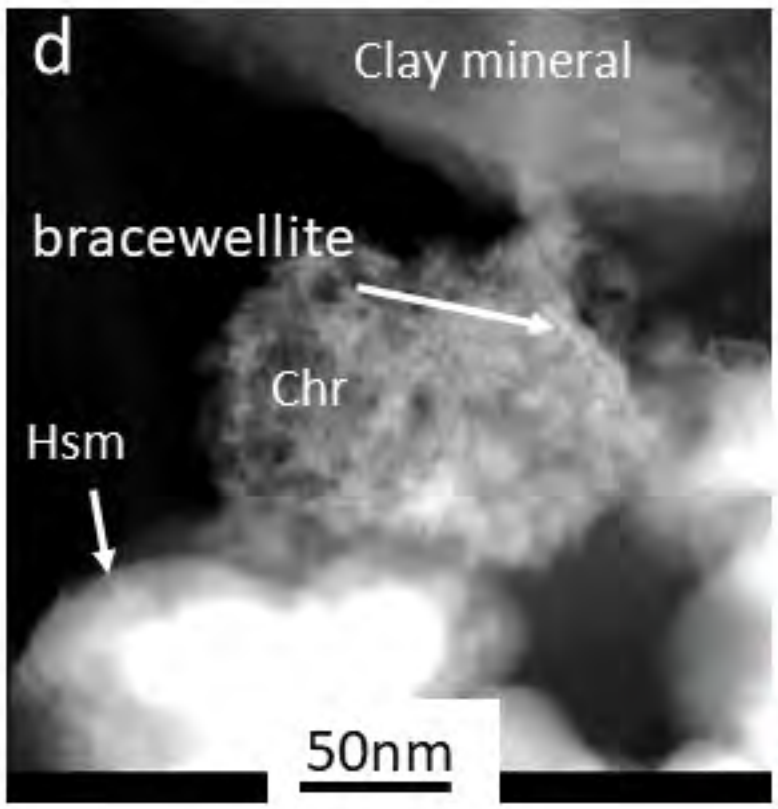
d
Clay mineral
bracewellite
Chr
Hsm
50nm

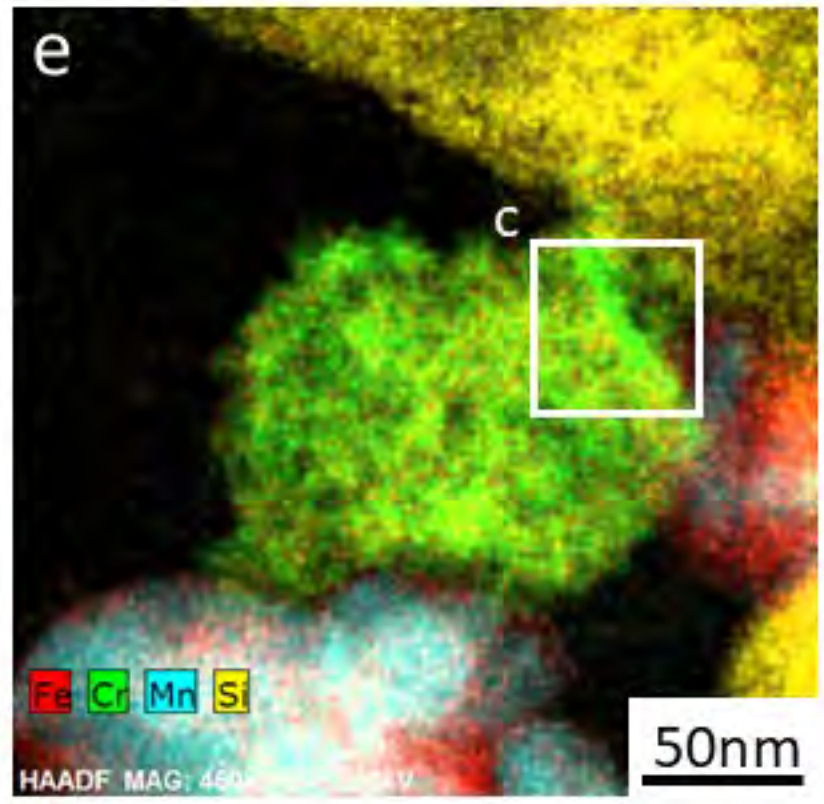
e
c
Fe Cr Mn Si
50nm

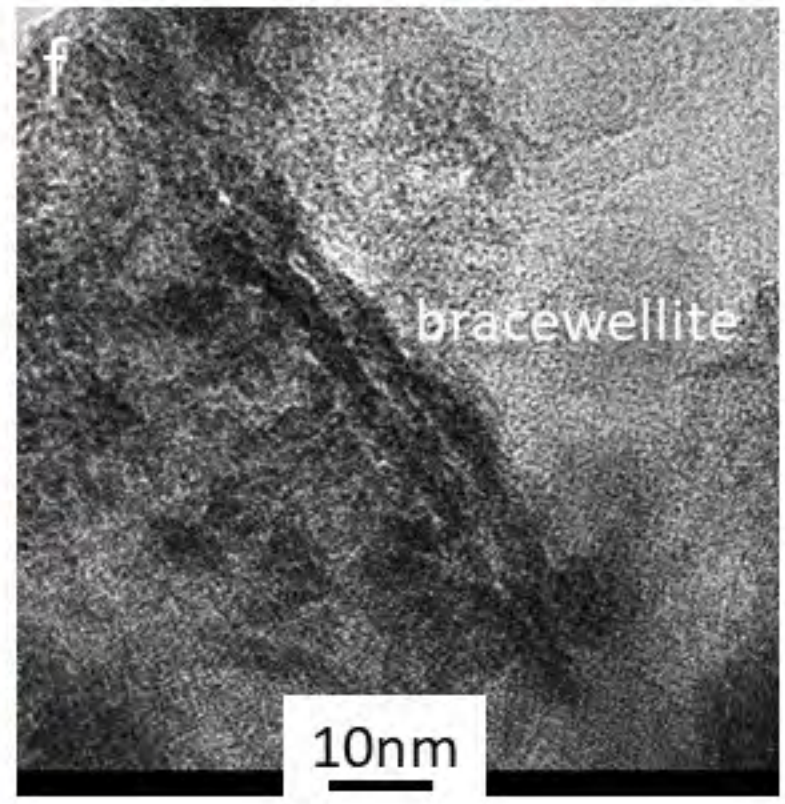
f
bracewellite
10nm

Figure 6

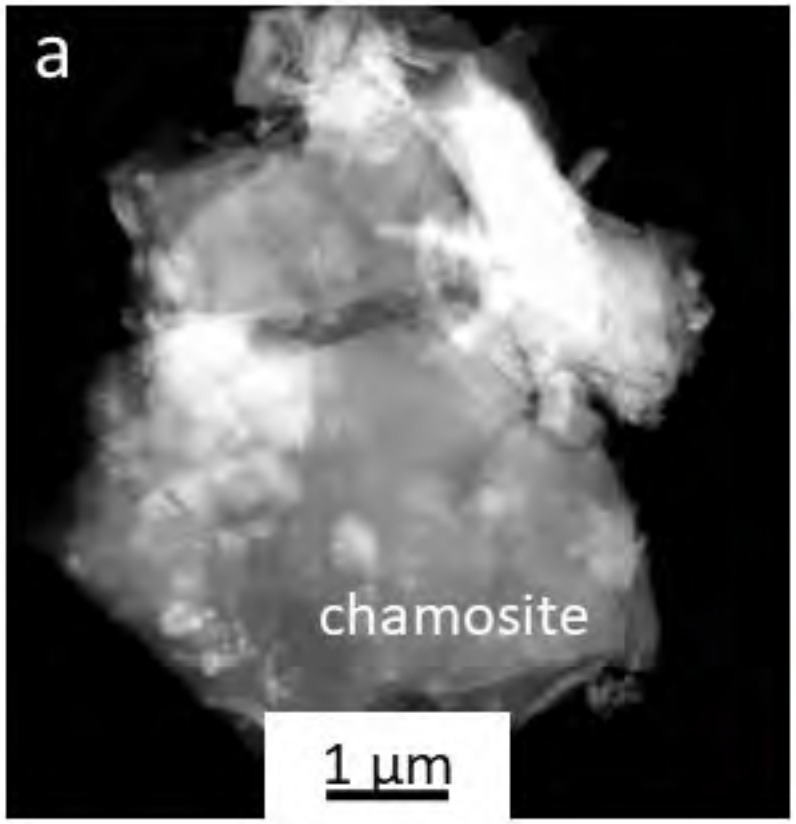
a
chamosite
1 µm

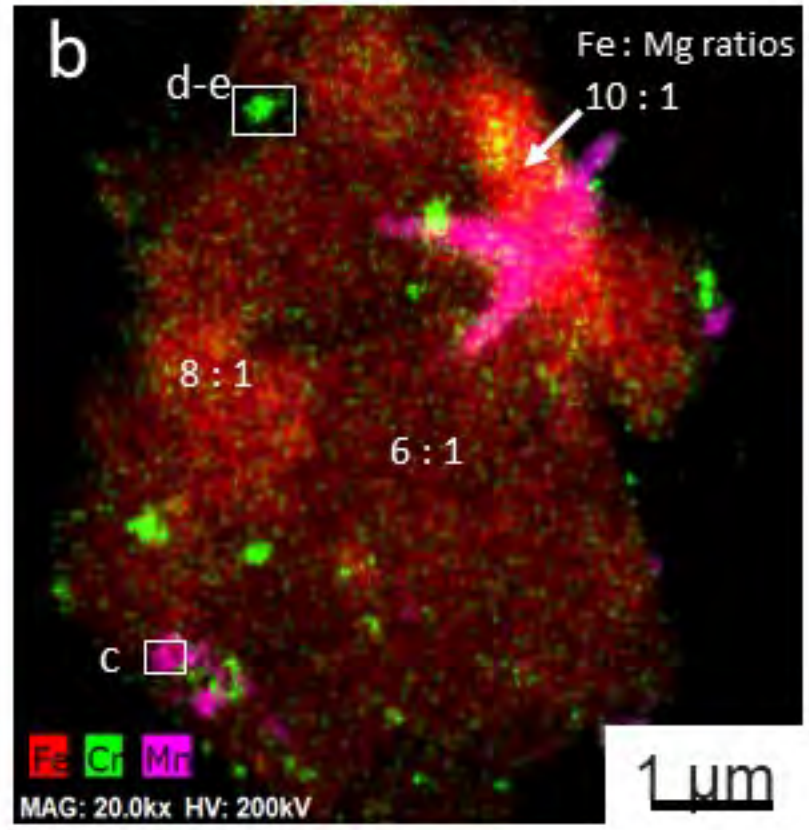
b
d-e
Fe : Mg ratios
10 : 1
8 : 1
6 : 1
c
Fe Cr Mn
MAG: 20.0kx HV: 200kV
1 µm

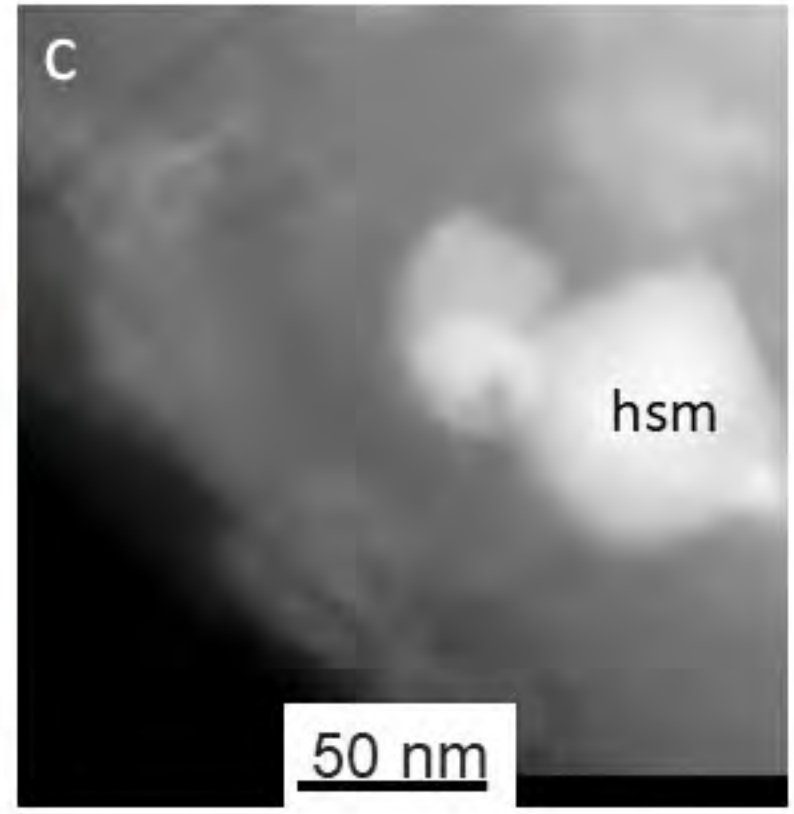
c
hsm
50 nm

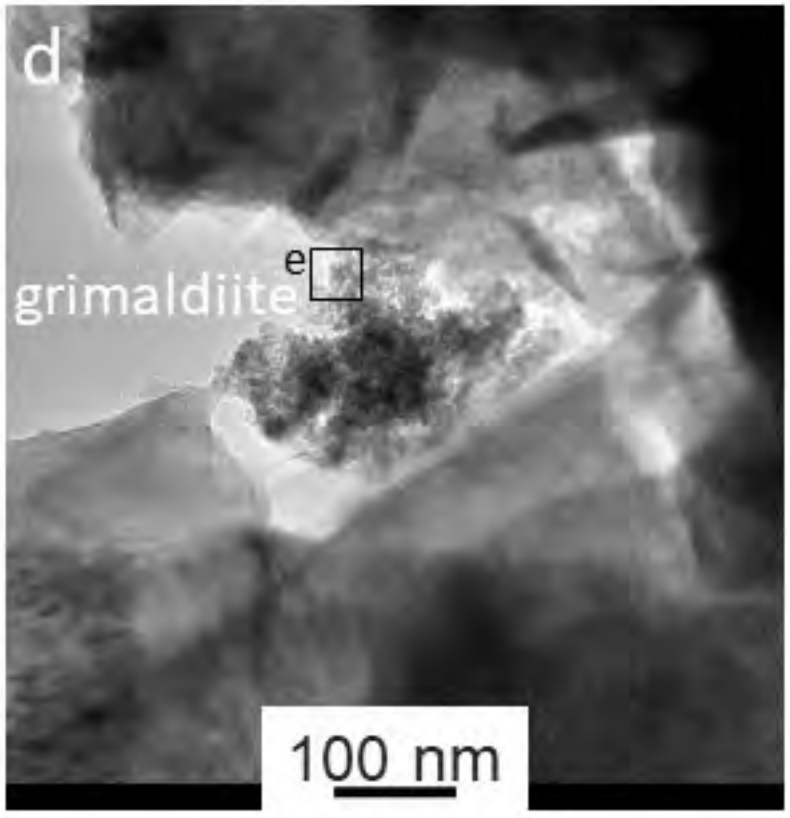
d
e
grimaldiite
100 nm

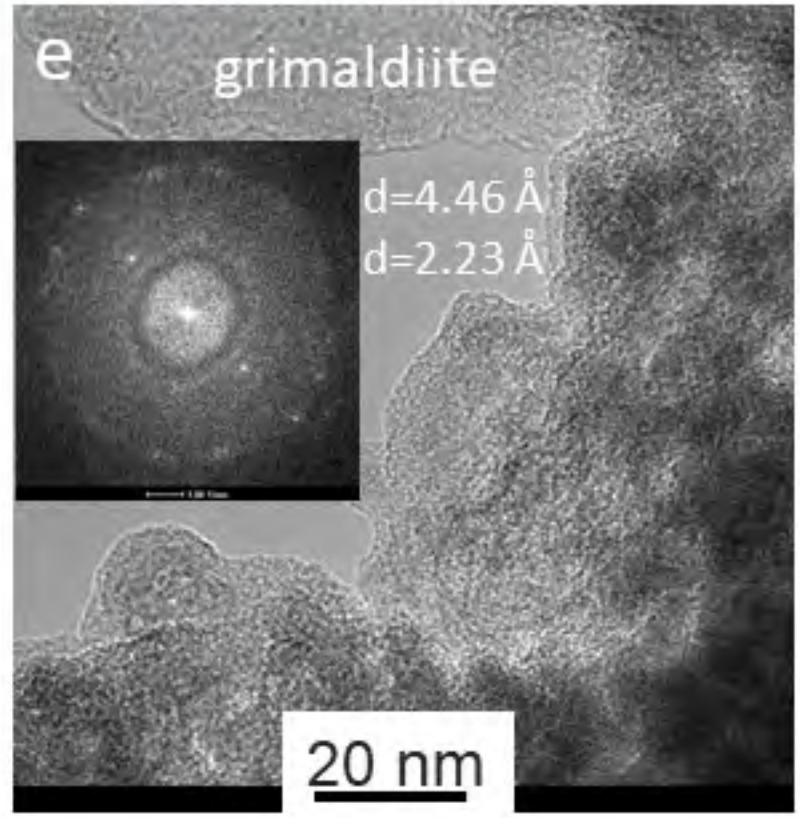
e
grimaldiite
d=4.46 Å
d=2.23 Å
20 nm

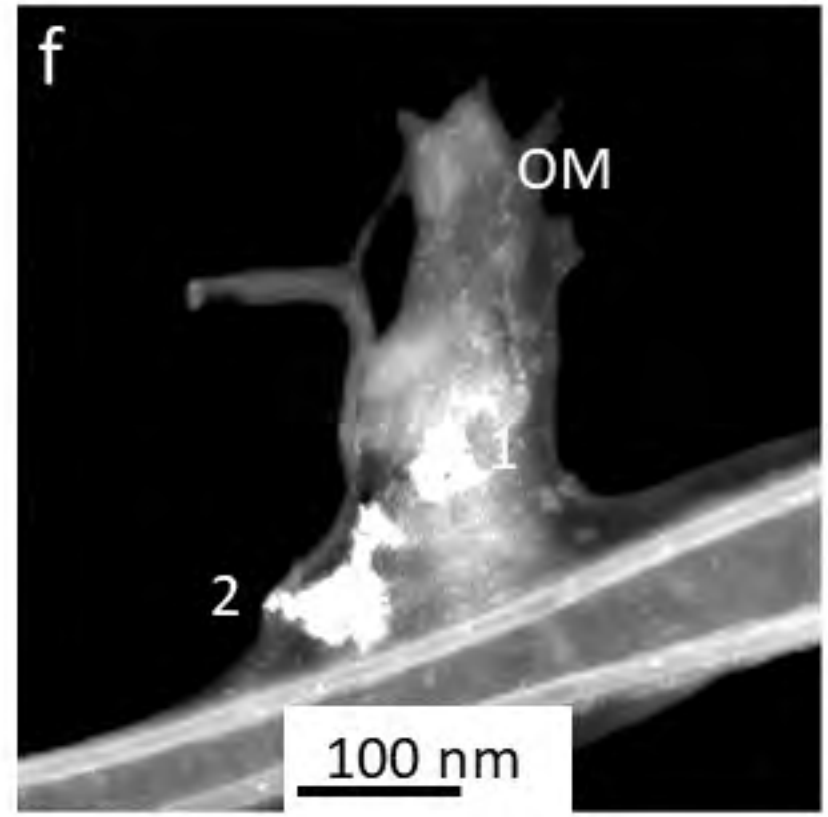
f
OM
1
2
100 nm

Figure 7